










Article

Structure-Based Identification of Natural Products as SARS-CoV-2 M^{Pro} Antagonist from *Echinacea angustifolia* Using Computational Approaches

Shiv Bharadwaj ¹, Sherif Aly El-Kafrawy ^{2,3}, Thamir A. Alandijany ^{2,3}, Leena Hussein Bajrai ^{2,4},
Altat Ahmad Shah ⁵, Amit Dubey ⁶, Amaresh Kumar Sahoo ⁷, Umesh Yadava ⁸, Mohammad Amjad Kamal ^{2,9},
Esam Ibraheem Azhar ^{2,3,*}, Sang Gu Kang ^{1,*} and Vivek Dhar Dwivedi ^{10,*}

- ¹ Department of Biotechnology, Institute of Biotechnology, College of Life and Applied Sciences, Yeungnam University, 280 Daehak-Ro, Gyeongsan, Gyeongbuk 38541, Korea; shiv@ynu.ac.kr
- ² Special Infectious Agents Unit, King Fahd Medical Research Center, King Abdulaziz University, 21589 Jeddah, Saudi Arabia; saelkafrawy@kau.edu.sa (S.A.E.-K.); talandijany@kau.edu.sa (T.A.A.); lbajrai@kau.edu.sa (L.H.B.); prof.ma.kamal@gmail.com (M.A.K.)
- ³ Department of Medical Laboratory Technology, Faculty of Applied Medical Sciences, King Abdulaziz University, Jeddah 21589, Saudi Arabia
- ⁴ Biochemistry Department, Faculty of Sciences, King Abdulaziz University, Jeddah 21589, Saudi Arabia
- ⁵ Department of Biosciences, Integral University, Lucknow 226026, India; altat.bioinfo321@gmail.com
- ⁶ Computational Chemistry and Drug Discovery Division, Quanta Calculus Pvt. Ltd., Kushinagar 274203, India; ameebioinfo@gmail.com
- ⁷ Department of Applied Sciences, Indian Institute of Information Technology Allahabad, Allahabad 211015, Uttar Pradesh, India; asahoo@iiti.ac.in
- ⁸ Department of Physics, Deen Dayal Upadhyay Gorakhpur University, Gorakhpur 273009, India; u_yadava@yahoo.com
- ⁹ Enzymoics, 7 Peterlee Place, Novel Global Community Educational Foundation, Hebersham, NSW 2770, Australia
- ¹⁰ Centre for Bioinformatics, Computational and Systems Biology, Pathfinder Research and Training Foundation, Greater Noida 201308, India
- * Correspondence: eazhar@kau.edu.sa (E.I.A.); kangsg@ynu.ac.kr (S.G.K.); vivek_bioinformatics@yahoo.com (V.D.D.)



Citation: Bharadwaj, S.; El-Kafrawy, S.A.; Alandijany, T.A.; Bajrai, L.H.; Shah, A.A.; Dubey, A.; Sahoo, A.K.; Yadava, U.; Kamal, M.A.; Azhar, E.I.; et al. Structure-Based Identification of Natural Products as SARS-CoV-2 M^{Pro} Antagonist from *Echinacea angustifolia* Using Computational Approaches. *Viruses* **2021**, *13*, 305. <https://doi.org/10.3390/v13020305>

Academic Editors:

Kenneth Lundstrom and Alaa A. A. Aljabali

Received: 12 January 2021

Accepted: 10 February 2021

Published: 15 February 2021

Publisher's Note: MDPI stays neutral with regard to jurisdictional claims in published maps and institutional affiliations.



Copyright: © 2021 by the authors. Licensee MDPI, Basel, Switzerland. This article is an open access article distributed under the terms and conditions of the Creative Commons Attribution (CC BY) license (<https://creativecommons.org/licenses/by/4.0/>).

Abstract: Coronavirus disease-19 (COVID-19) pandemic, caused by the novel SARS-CoV-2 virus, continues to be a global threat. The number of cases and deaths will remain escalating due to the lack of effective therapeutic agents. Several studies have established the importance of the viral main protease (M^{Pro}) in the replication of SARS-CoV-2 which makes it an attractive target for antiviral drug development, including pharmaceutical repurposing and other medicinal chemistry approaches. Identification of natural products with considerable inhibitory potential against SARS-CoV-2 could be beneficial as a rapid and potent alternative with drug-likeness by comparison to de novo antiviral drug discovery approaches. Thereof, we carried out the structure-based screening of natural products from *Echinacea-angustifolia*, commonly used to prevent cold and other microbial respiratory infections, targeting SARS-CoV-2 M^{Pro}. Four natural products namely, Echinacoside, Quercetagenin 7-glucoside, Levan N, Inulin from chicory, and 1,3-Dicaffeoylquinic acid, revealed significant docking energy (>−10 kcal/mol) in the SARS-CoV-2 M^{Pro} catalytic pocket via substantial intermolecular contacts formation against co-crystallized ligand (<−4 kcal/mol). Furthermore, the docked poses of SARS-CoV-2 M^{Pro} with selected natural products showed conformational stability through molecular dynamics. Exploring the end-point net binding energy exhibited substantial contribution of Coulomb and van der Waals interactions to the stability of respective docked conformations. These results advocated the natural products from *Echinacea angustifolia* for further experimental studies with an elevated probability to discover the potent SARS-CoV-2 M^{Pro} antagonist with higher affinity and drug-likeness.

Keywords: SARS-CoV-2; COVID-19; natural products; *Echinacea-angustifolia*; molecular dynamics simulation; Quercetagenin 7-glucoside

1. Introduction

Coronavirus disease 2019 (COVID-19) is caused by a novel positive-sense single-stranded RNA virus named severe acute respiratory syndrome coronavirus-2 (SARS-CoV-2). This virus has been classified under family Coronaviridae, subfamily *Coronaviridae* and order *Nidovirales* [1]. More than 69.8 million cases have been reported globally and have resulted in the death of more than 1.4 million people as of December 2020 [2]. The disease is associated with highly variable symptoms ranging from mild ones like fever, cough, and sneezing to severe life-threatening complications (e.g., acute respiratory distress syndrome and multiple organ failure). The RNA genome sequence of SARS-CoV-2 is about 30 kb in size that encodes a large polyprotein. Later, the polyprotein is digested into 4 structural proteins, such as spike (S), envelope (E), membrane (M), and nucleocapsid (N) as well as 16 non-structured proteins (nsp1–nsp16), and 8 accessory proteins. Each SARS-CoV-2 protein has its unique and key functions in the viral replication cycle. The viral protein nsp5, also termed as 3C-like proteinase (3CL^{pro}) or main protease (M^{pro}), is a key for processing of polyprotein into the functional proteins [3]. Hence, it has been recognized as an important anti-SARS-CoV-2 target due to its essential role in viral replication. Indeed, targeting and inhibiting the activity of M^{pro} might block or impair viral replication [4]. Several crystallographic and nuclear magnetic resonance (NMR) structures of SARS-CoV-2 M^{pro} have been solved in complex with different small molecules [3,5], which is critical achievement in discovering new therapeutics against COVID-19. However, there is no specialized prophylaxis or treatment for this virus till date, therefore, it demands an urgent requirement for the screening of new potent and effective drugs against SARS-CoV-2 [6].

In the area of drug discovery research, medicinal plants are one of the most popular sources of effective natural lead molecules. They contain a variety of phytochemicals that can be used as a drug against different diseases and infections [7]. There are several reports on the antiviral activity of numerous plants against highly pathogenic viruses, including coronaviruses [8,9]. The plants of *Echinacea* genus are one among those plants, which are well known for their potential antiviral activity against pathogenic coronaviruses [10–13]. *Echinacea angustifolia* (*E. angustifolia*) is one of the popular medical plants belonging to this genus with medicinal value, including antimicrobial and anti-inflammatory activities [14,15]. *E. angustifolia* have been reported to exhibited broad-spectrum antibacterial activity for several Gram-positive and Gram-negative bacteria like *Escherichia coli*, *Staphylococcus aureus*, *Bacillus subtilis*, and *Staphylococcus epidermidis* [16]. Interestingly, the antiviral activity of *E. angustifolia* is well known against several viruses like herpes simplex virus (HSV), influenza virus (FV), and rhinovirus (RV) [17]. Hence, this study was designed to identify the natural products in *E. angustifolia* with considerable potential to treat SARS-CoV-2 infection via SARS-CoV-2 M^{pro} inhibition. In this context, structure-based drug discovery methods, including molecular docking simulation, molecular dynamics (MD) simulation, and end point binding free energy approach were used to assess the therapeutic potential of natural products in *E. angustifolia* against SARS-CoV-2 by targeting M^{pro} protein as depicted in Figure 1.

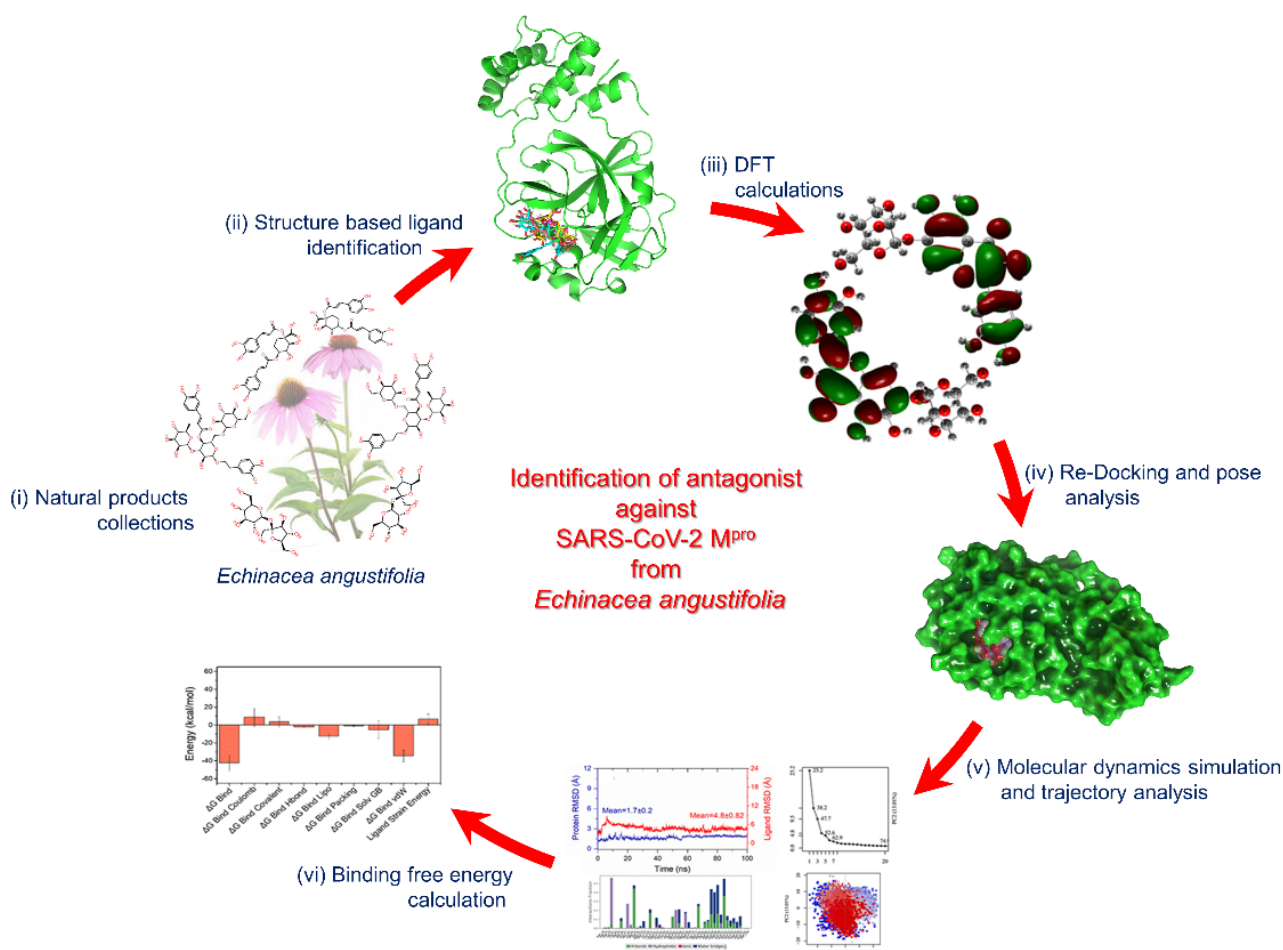


Figure 1. Computational assessment of natural products in *E. angustifolia* against SARS-CoV-2 M^{Pro}. Herein, (i) 3D structures of natural products reported in *E. angustifolia* were retrieved from the PubChem database, (ii) these natural products were then screened into the active region of SARS-CoV-2 M^{Pro} by XP docking, (iii) natural products with highest negative docking energy were collected and treated by DFT method for respective geometry optimization to calculate other molecular properties, (iv) these optimized geometries of natural products were re-docked with SARS-CoV-2 M^{Pro} and studied for pose binding and molecular contacts formation, (v) best docked poses were further studied for stability and protein ligand contact formation as function of 100 ns interval, and (vi) frames were extracted from respective MD trajectories and used in binding free energy calculations.

2. Methodology

2.1. Receptor and Ligands Collection

Three-dimensional (3D) X-ray crystal structure of SARS-CoV-2 M^{Pro} (PDB ID: 5R82) [18] co-crystallized with 6-(ethylamino)pyridine-3-carbonitrile at 1.31 Å resolution was downloaded as receptor from the RCSB protein database (<http://www.rcsb.org/pdb/home/home.do>) (accessed on 10 January 2021) [19]. Besides, the natural products reported in *Echinacea angustifolia* were collected from the literature and their respective 2D or 3D structures were downloaded in ‘sdf’ format from the PubChem database (<https://pubchem.ncbi.nlm.nih.gov>) (accessed on 10 January 2021) [20].

2.2. Structure-Based Ligand Identification and Quantum Chemical Calculations

Initially, 2D and 3D structures of the collected natural products reported in *E. angustifolia* were prepared for the molecular docking using LigPrep module in the Schrödinger suite (Schrödinger Release 2019-2: LigPrep, Schrödinger, LLC, New York, NY, USA, 2019). Moreover, the crystal structure of SARS-CoV-2 M^{Pro} was also refined for the molecular

docking using PRIME and protein preparation wizards in Schrödinger suite (Schrödinger Release 2019.2: Prime, Schrödinger, LLC, New York, NY, USA, 2019). For the identification of natural products from *E. angustifolia* with the potential to block SARS-CoV-2 M^{PRO}, the active residues (His⁴¹, Ser⁴⁶, Met⁴⁹, Cys¹⁴⁵, His¹⁶⁴, Met¹⁶⁵, Phe¹⁸¹, Asp¹⁸⁷, Arg¹⁸⁸, and Gln¹⁸⁹) interacting with the co-crystallized ligand, i.e., 6-(ethylamino)pyridine-3-carbonitrile, were considered in the molecular docking method, as described in crystal structure of SARS-CoV-2 M^{PRO} [18]. Next, molecular docking simulation was performed under default parameters using extra precision (XP) protocol of the GLIDE tool in Schrödinger suite (Schrödinger Release 2019.2: Glide, Schrödinger, LLC, New York, NY, USA, 2019). During this process, receptor was treated as a rigid entity while ligands were considered as flexible to attain the most feasible interactions with the active residues in the catalytic pocket of SARS-CoV-2 M^{PRO}. Additionally, polar interactions, Coulombic, hydrogen bond, hydrophobic contacts, van der Waals, metal binding, freezing rotatable bonds, water desolvation energy, binding affinity enriching interactions, and the penalty for buried polar groups were also considered in the Glide extra precision (XP) scoring approach [21]. Following, ligands exhibiting highest negative docking score in SARS-CoV-2 M^{PRO} catalytic pocket were considered for further structure refinement using the quantum chemical calculation in GAUSSIAN-03 suite [22]. The selected natural products along with co-crystallized ligand as a reference compound, i.e., 6-(ethylamino)pyridine-3-carbonitrile, were treated with the density functional theory (DFT) [23] under hybrid functional Becke's three-parameter and the Lee–Yang–Parr functional (B3LYP) [24,25] in conjunction with 6-31G(d,p) basis sets, as reported earlier [26]. The molecular geometries of each natural product as ligand were fully optimized without constraint and respective global minima for the potential energy surface of each ligand were calculated devoid of imaginary frequency modes. Later, the computed optimized geometries were further studied for the molecular properties using GAUSSIAN-03 suite [22].

2.3. Re-Docking Simulation and Pose Profiling

The DFT optimized geometries of the natural products were re-docked in the catalytic pocket of SARS-CoV-2 M^{PRO} using extra precision (XP) protocol of the GLIDE module in Schrödinger suite, as discussed in the earlier section. Next, at least 10 poses were generated for each docked ligand with SARS-CoV-2 M^{PRO} and binding pose with highest negative docking score corresponds to least root mean square deviation (RMSD) were collected for intermolecular interactions in the academic Schrödinger-Maestro v12.4 suite (Schrödinger Release 2020-2: Maestro, Schrödinger, LLC, New York, NY, USA, 2020). Molecular contacts formed between the ligands and active residues of SARS-CoV-2 M^{PRO} were evaluated within 4 Å area around the ligand in terms of noncovalent interactions, viz. hydrophobic interactions, hydrogen bonding, π - π interactions, π -cation interactions, positive interactions, negative interactions, glycine interactions, and formation of salt bridges under default parameters. Likewise, optimized co-crystallized ligand, i.e., 6-(ethylamino)pyridine-3-carbonitrile, was also docked in the binding region of SARS-CoV-2 M^{PRO} to validate the docking protocol and for comparative analysis against selected natural products. Later, both 3D and 2D docked poses of viral protease with natural products were rendered in the academic Schrödinger-Maestro v12.4 suite (Schrödinger Release 2020-2: Maestro, Schrödinger, LLC, New York, NY, USA, 2020).

2.4. Explicit Solvent Molecular Dynamics Simulations

The best-docked poses of SARS-CoV-2 M^{PRO}-natural products were considered for molecular dynamics (MD) simulation analysis to envisage the stability of the selected docked complexes and intermolecular interaction as function of 100 ns time under a Linux environment on an HP Z2 Microtower workstation by academic version of Desmond v5.6 module [27] through Schrödinger-Maestro v11.8 suite interface (Schrödinger Release 2018-4: Desmond Molecular Dynamics System, D. E. Shaw Research, New York, NY, USA, 2018. Maestro-Desmond Interoperability Tools, Schrödinger, New York, NY, USA,

2018). Each docked complex was initially refined using the Protein preparation wizard and later covered in an orthorhombic grid box ($10 \times 10 \times 10 \text{ \AA}$ buffer) amended with TIP4P (transferable intermolecular potential 4 points) water bath. The explicit solvent was selected for the MD simulation to recover most of the solvation effects of real solvent, including a contribution from the entropic origin such as the hydrophobic effect. In addition, counter Na^+ and Cl^- ions were amended to nullify the charge of the whole system while placed at a distance of 20 \AA around the ligand with the aid of a system builder tool. Additionally, salt of 0.15 M concentration was amended into the system to mimic the physiological conditions. Following, initial minimization of the whole system was performed under default parameters. This was followed by 100 ns molecular dynamics (MD) simulation at 300 K with default parameters. Finally, MD simulation trajectories collected at every 10 ps were analyzed for each simulated complex using the simulation interaction diagram (SID) tool of Desmond v5.6 package in Schrödinger-Maestro v11.8 suite.

2.5. Post Molecular Dynamics Simulation

2.5.1. Essential Dynamics

Essential dynamics, in terms of principal component analysis (PCA), assisted in the collection of concerted motions linked with the largest atomic vibrations that are essentially required for the protein function [28,29]. Typically, $>90\%$ of the exhibited total atomic fluctuations can be defined by $\approx 20\%$ of the principal axes, i.e., the covariance matrix eigenvectors [29]. Essential dynamics analysis was conducted on the respective MD simulation trajectories to assemble the PCs using Bio3d package [30]. The extraction of PCs was conducted based on all the $\text{C}\alpha$ atoms of 5000 snapshots extracted from 100 ns MD simulation trajectory and aligned to the docked conformation pose to nullify the root mean square deviation (RMSD) between corresponding residues of the protein conformations. All the computations were performed on each simulated complex MD trajectory with the Bio3d package [30] under the R program environment [31].

2.5.2. Binding Free Energy Calculations

In this study, binding free energy calculation was conducted using molecular mechanics generalized Born surface area (MM/GBSA), which is comparatively popular and more accurate approach against scoring function of molecular docking as well as computationally less demanding with respect to alchemical free energy methods [32]. Hence, net binding energy calculation were conducted using Prime MM/GBSA module by MM/GBSA protocol, as described earlier [33,34]. Herein, protein-ligand complex generated following molecular docking and snapshots extracted from 100 ns MD simulation trajectory (without explicit TIP4P water molecules and ions) for each complex was considered for net binding free energy calculation. The Equations (1)–(3) represents the mathematical expression to express the end-point binding free energy and respective individual decomposed energy components:

$$\Delta G_{\text{Bind}} = \Delta G_{\text{Com}} - (\Delta G_{\text{Rec}} + \Delta G_{\text{Lig}}) = \Delta H - T\Delta S \approx \Delta E_{\text{MM}} + \Delta G_{\text{Sol}} - T\Delta S, \quad (1)$$

$$\Delta E_{\text{MM}} = \Delta E_{\text{Int}} + \Delta E_{\text{Ele}} + \Delta E_{\text{vdW}}, \quad (2)$$

$$\Delta G_{\text{Sol}} = \Delta G_{\text{Pol}} + \Delta E_{\text{Nonpol}}. \quad (3)$$

The net binding free energy (ΔG_{Bind}) is defined as the sum of free energy difference between the protein-ligand complex (G_{Com}) and the free-state of each protein and ligand ($G_{\text{Rec}} + G_{\text{Lig}}$). As the second law of thermodynamics stated, total binding free energy (ΔG_{Bind}) of the protein-ligand complex is the sum of the enthalpy part (ΔH) and the entropy part ($-T\Delta S$) of the complete system, as given in Equation (1).

To note, available computational methods for entropy calculation for the protein-ligand complex, including varying from post-processing methodologies [35–39] to the simulation-synchronized approaches [40–42], essentially required hundreds of nanoseconds simulation trajectories to explicitly compute the system entropy and such method-

ologies are only tested on a small system containing a few hundreds of atoms. Previous studies have suggested that these computational methodologies are not accessible to calculate the entropy of a system composed of thousands of atoms such as the protein-ligand complex [43]. Thus, contribution of entropy in the present study to calculate the net binding energy for the protein-ligand complexes was dropped due to high computational cost and relatively low contribution in total binding free energy, as reported earlier [43]. Given these conditions, enthalpy of the system can be assigned equal to the total binding free energy of the protein-ligand complex; and hence, expressed as the sum of molecular mechanical energy (ΔE_{MM}) and solvation free energy (ΔG_{Sol}). Characteristically, ΔE_{MM} is defined as the sum of intramolecular energy (ΔE_{Int} , which is the addition of the bond, angle, bond, and dihedral energies), the electrostatic energy (ΔE_{Ele}), and the van der Waals interactions (ΔE_{vdW}). Likewise, ΔG_{Sol} is the addition of net polar energy (ΔG_{Pol}) and non-polar (ΔE_{Nonpol}) of the system. Thus, total binding free energy were calculated using the MM/GBSA approach for each complex under default parameters with OPLS-2005 force field on the last 10 ns intervals of each 100 ns MD simulation trajectories.

3. Results and Discussion

3.1. Structure-Based Ligand Identification

Molecular docking simulation is a widely used computational approach in drug discovery. It enables discovering the favorable ligands with ideal conformation in the binding pocket of the target proteins. In this context, the XP docking algorithm in Glide aids in the identification of ligands with high affinities in the binding pocket of the receptor by including water desolvation energy, hydrophobic interactions, generation of neutral-neutral single or interrelated hydrogen bonds in a hydrophobically restricted environment, and other five clusters of charged-charged hydrogen bond formation [21]. Herein, a total of 50 natural products reported in *E. angustifolia* were docked in the binding pocket of viral main protease (M^{Pro}) using the Glide XP protocol, yields ligands with binding affinities in the range of -12.93 to 0.0897 kcal/mol, at least docking RMSD values as shown in Table S1. One of the main objectives of this study was to identify the ideal poses of the docked ligands based on their docking score which can block the target protein. Hence, top five natural products, i.e., Echinacoside, Quercetagenin 7-glucoside, Levan N, Inulin from chicory, and 1,3-Dicaffeoylquinic acid, docked with SARS-CoV-2 M^{Pro} were considered for further intermolecular interaction analysis.

Echinacoside (ECH), a natural phenylethanoid glycoside, has been investigated for numerous pharmacologically benefits possessing high antiviral activities (e.g., against vesicular stomatitis virus) [44], and limited immune activation properties [45]. Whereas Levan is characterized as a naturally occurring polymer of fructan and typified by β -(2,6) linkages, and commonly present with diverse degree of polymerization in many microorganisms and plants species [46,47]. Levan isolated from *Bacillus* sp. strains showed antiviral activity against pathogenic avian influenza HPAI, H5N1, and adenovirus type 40 [48]. Remarkably, both H5N1 and SARS-CoV are RNA viruses that cause severe viral pneumonia leading to ARDS [49]. Likewise, Inulin is also a fructose polymer and differentiate from the Levan based on β -(2,1) bonds linkages. Unlike Levan, Inulin is only known for indirect viral inhibition by promoting and regulating the immune system [50]. Of note, a fructan composed of terminal (21.0%) and 2,1-linked β -d-Fruf residues (65.3%) with 1,6-linked β -d-Glcp residues (13.7%) isolated from Welsh onion (*Allium fistulosum* L.) was documented for in vivo inhibitory effect on influenza A virus replication [51]. Furthermore, 1,3-Dicaffeoylquinic acid (Cynarin) isolated from *Inula viscosa* was reported for exhibiting strong antioxidant activities via direct scavenging of several free radicals [52] while 1,3-Dicaffeoylquinic acid extracted from the leaves of *Cynara cardunculus* L. (Asteraceae) exhibited the inhibition of HIV-1 replication in MT-2 cell culture at non-toxic concentrations [53]. Recently, screening of anti-influenza lead compounds also identified a 1,3-Dicaffeoylquinic acid as an inhibitor of viral RNA polymerase [54]. Based on these reported literatures, it was concluded that

the selected natural products possess medical properties, including antiviral activities; and hence, can be processed for further analysis within the catalytic pocket of SARS-CoV-2 M^{Pro}.

3.2. Quantum Chemical Calculations

3.2.1. Geometry Optimization

To calculate the molecular properties of the ligand in computational chemistry, hybrid functional B3LYP with 6-31(d,p) basis is well established for the geometry optimization of organic compounds. In this study, initially geometry optimization was performed and then structural parameters, including bond angles, dihedral angles, and bond length, were studied for the selected natural products, i.e., Echinacoside, Quercetagetin 7-glucoside, Levan N, Inulin from chicory, and 1,3-Dicaffeoylquinic acid, from *E. angustifolia* as antagonist against SARS-CoV-2 M^{Pro} along with co-crystallized ligand 6-(ethylamino)pyridine-3-carbonitrile as reference compound (Tables S2–S7). Figure 2 shows the 2D structure and 3D optimized geometries labeled with atom number scheme for the selected natural products and reference compound, which were rendered using GaussView 3.0.8.

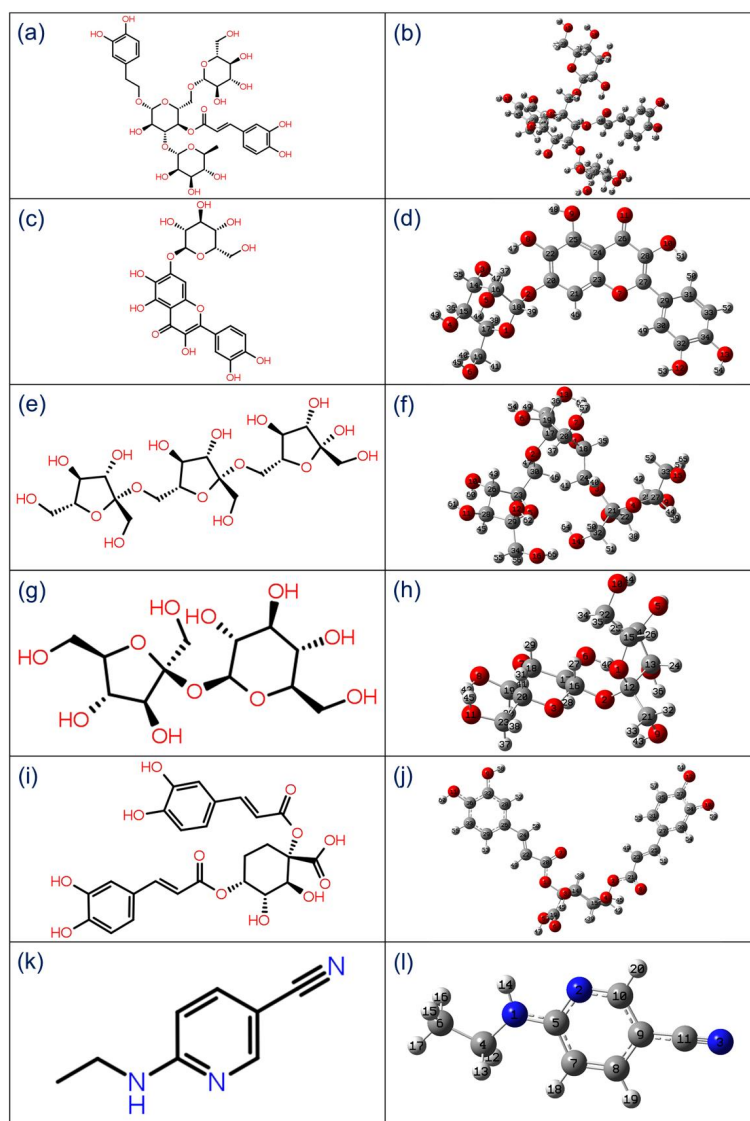


Figure 2. 2D structures and 3D optimized molecular geometries of natural products, viz. (a,b) Echinacoside, (c,d) Quercetagetin 7-glucoside, (e,f) Levan N, (g,h) Inulin from chicory, (i,j) 1,3-Dicaffeoylquinic acid, and (k,l) 6-(ethylamino) pyridine-3-carbonitrile as reference compound, were calculated using DFT/B3LYP/6-31G(d,p) level.

3.2.2. Frontier Molecular Orbitals Analysis

In chemical reactions, the interaction and overlapping of two reactants' molecular orbitals results leads to the formation of two new molecular orbitals, i.e., one as bonding orbitals containing less bonding energy and another as antibonding with higher energy [55]. Thus, the energy difference in the highly occupied molecular orbital (HOMO) and lower unoccupied molecular orbitals (LUMO), viz. $E_{\text{HOMO}}-E_{\text{LUMO}}$, for a chemical species, can be used to calculate its kinetic stability, chemical reactivity, and hardness [56,57]. Interestingly, a decrease in the frontier molecular orbital energy gap also indicates the intermolecular charge transfer (ICT) from donors to acceptor atoms and assist to elucidate the bioactivity of the molecule. Thereof, E_{HOMO} , E_{LUMO} , and $E_{\text{HOMO}}-E_{\text{LUMO}}$ values were computed from optimized geometries of the selected natural products. Figure 3 exhibits the asymmetric frontier molecular orbitals, i.e., HOMO and LUMO, for the potential natural products, i.e., (a) Echinacoside, (b) Quercetagenin 7-glucoside, (c) Levan N, (d) Inulin from chicory, and (e) 1,3-Dicaffeoylquinic acid. Herein, red and green color distribution was observed around the electronegative and electropositive atoms, respectively, demonstrates the corresponding negative and positive phases of the molecular frontier orbital wave function in the selected natural products. Likewise, reference compound 6-(ethylamino) pyridine-3-carbonitrile studied for the distribution of frontier molecular orbitals indicate formation of asymmetric HOMO and LUMO over electronegative and electropositive atoms on the optimized geometry (Figure S1). Hence, the electronegative and positive atoms in the respective ligand structures were predicted for formation of donor and acceptor molecular contacts in the active pocket of viral protease during molecular docking simulation. Furthermore, computed energy gap for the selected natural products also indicates the considerable kinetic stability and low chemical reactivity against reference compound (Figure 3 and Figure S1). To note, Levan N (6.57 eV) and Inulin from chicory (5.98 eV) showed higher energy gap by comparison to other selected natural products, i.e., Echinacoside (4.04 eV), Quercetagenin 7-glucoside (3.98 eV), 1,3-Dicaffeoylquinic acid (4.02 eV), and reference compound 6-(ethylamino)pyridine-3-carbonitrile (5.77 eV), suggested their substantial bioactivity and potential as antagonists against SARS-CoV-2 M^{Pro}. Conclusively, these observations suggested the considerable unreactive chemical behavior and chemical stability for the selected natural products, i.e., Echinacoside, Quercetagenin 7-glucoside, Levan N, Inulin from chicory and 1,3-Dicaffeoylquinic acid, against reference compound 6-(ethylamino) pyridine-3-carbonitrile.

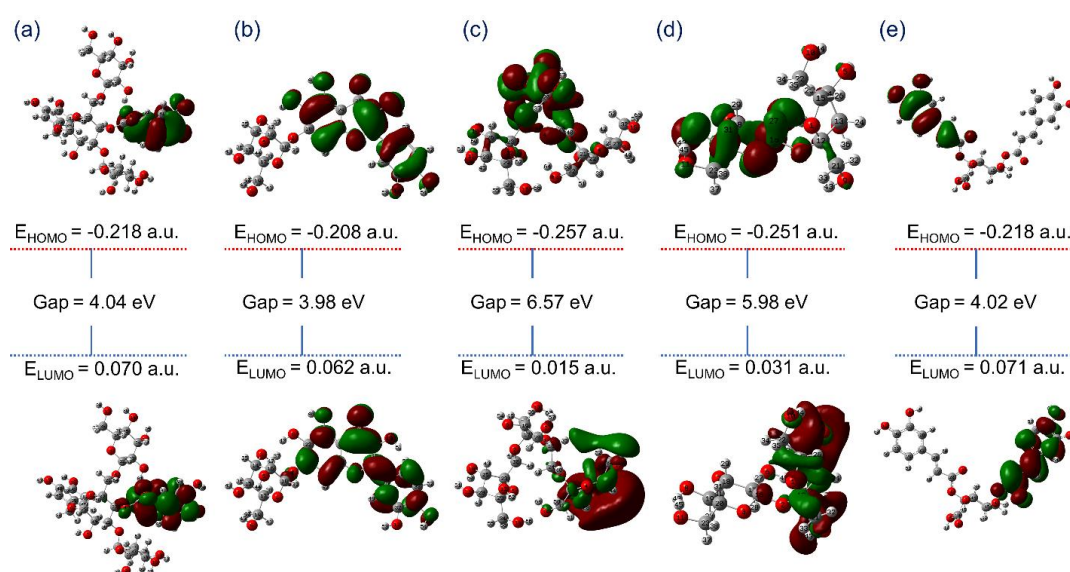


Figure 3. Molecular orbitals, i.e., highly occupied molecular orbital (HOMO) and lower unoccupied molecular orbitals (LUMO) of the optimized geometries of selected natural compounds, viz. (a) Echinacoside, (b) Quercetagenin 7-glucoside, (c) Levan N, (d) Inulin from chicory, and (e) 1,3-Dicaffeoylquinic acid, calculated using theoretical model B3LYP/6-31G** method.

3.3. Re-Docking and Intermolecular Interaction Analysis

The DFT optimized structures of the potential natural products were further analyzed by re-docking in the catalytic pocket of SARS-CoV-2 M^{PRO} to monitor the intermolecular interactions that can contribute to the stability of the respective docked complexes. Thus, selected natural products and reference ligand, viz. 6-(ethylamino) pyridine-3-carbonitrile, were re-docked in SARS-CoV-2 M^{PRO} catalytic pocket by XP docking protocol. Following, the docked poses with highest negative docking score were considered for intermolecular interaction analysis. (Table 1, Figure 4, Figure S2).

Table 1. Intermolecular interactions observed for the best poses of docked natural products against reference compounds in the catalytic pocket of SARS-CoV-2 M^{PRO} against the reference ligand.

S. no.	Compound	Docking Score (kcal/mol)	H-Bond	π - π / * π -Cation Stacking	Hydrophobic	Polar	Negative	Positive	Glycine/ * Salt Bridge
1	Echinacoside	-14.17	Thr ²⁵ , Cys ⁴⁴ , Asn ¹⁴² , Gly ¹⁴³ , Gln ¹⁸⁹ , Thr ¹⁹⁰	-	Leu ²⁷ , Val ⁴² , Cys ⁴⁴ , Met ⁴⁹ , Phe ¹⁴⁰ , Leu ¹⁴¹ , Cys ¹⁴⁵ , Met ¹⁶⁵ , Leu ¹⁶⁷ , Pro ¹⁶⁸ , Ala ¹⁹¹	Thr ²⁴ , Thr ²⁵ , His ⁴¹ , Thr ⁴⁵ , Ser ⁴⁶ , Asn ¹⁴² , Ser ¹⁴⁴ , His ¹⁶³ , His ¹⁶⁴ , His ¹⁷² , Gln ¹⁸⁹ , Thr ¹⁹⁰ , Gln ¹⁹²	Glu ¹⁶⁶	Arg ¹⁸⁸	Gly ¹⁴³
2	Quercetagenin 7-Glucoside	-15.20	Cys ⁴⁴ (2), Leu ¹⁴¹ , Cys ¹⁴⁵ , Glu ¹⁶⁶ (2), Gln ¹⁸⁹	* His ⁴¹	Leu ²⁷ , Cys ⁴⁴ , Met ⁴⁹ , Phe ¹⁴⁰ , Leu ¹⁴¹ , Cys ¹⁴⁵ , Met ¹⁶⁵ , Leu ¹⁶⁷ , Pro ¹⁶⁸	Thr ²⁴ , Thr ²⁵ , Thr ²⁶ , His ⁴¹ , Thr ⁴⁵ , Ser ⁴⁶ , Asn ¹⁴² , Ser ¹⁴⁴ , His ¹⁶³ , Gln ¹⁸⁹	Glu ¹⁶⁶	-	Gly ¹⁴³
3	Levan N	-12.92	His ⁴¹ , Cys ⁴⁴ , Asn ¹⁴² , Gly ¹⁴³ , Gln ¹⁸⁹ (3)	-	Val ⁴² , Cys ⁴⁴ , Met ⁴⁹ , Leu ¹⁴¹ , Cys ¹⁴⁵ , Met ¹⁶⁵	Thr ²⁴ , Thr ²⁵ , His ⁴¹ , Thr ⁴⁵ , Ser ⁴⁶ , Asn ¹⁴² , Ser ¹⁴⁴ , His ¹⁶⁴ , Gln ¹⁸⁹	Glu ¹⁶⁶	Arg ¹⁸⁸	Gly ¹⁴³
4	Inulin From Chicory	-11.72	Leu ¹⁴¹ , Gly ¹⁴³ , Glu ¹⁶⁶ (2), Gln ¹⁸⁹ (2)	-	Met ⁴⁹ , Phe ¹⁴⁰ , Leu ¹⁴¹ , Cys ¹⁴⁵ , Met ¹⁶⁵ , Leu ¹⁶⁷ , Pro ¹⁶⁸	His ⁴¹ , Asn ¹⁴² , Ser ¹⁴⁴ , His ¹⁶³ , His ¹⁶⁴ , Gln ¹⁸⁹ , Thr ¹⁹⁰ , Gln ¹⁹²	Glu ¹⁶⁶	Arg ¹⁸⁸	Gly ¹⁴³
5	1,3-Dicaffeoylquinic Acid	-10.01	Thr ²⁶ , Thr ²⁵ , Gly ¹⁴³ , Arg ¹⁸⁸ (2)	-	Leu ²⁷ , Cys ⁴⁴ , Met ⁴⁹ , Cys ¹⁴⁵ , Met ¹⁶⁵ , Leu ¹⁶⁷ , Val ¹⁸⁶	Thr ²⁴ , Thr ²⁵ , Thr ²⁶ , His ⁴¹ , Thr ⁴⁵ , Ser ⁴⁶ , Asn ¹⁴² , Ser ¹⁴⁴ , Gln ¹⁸⁹ , Thr ¹⁹⁰ , Gln ¹⁹²	Glu ¹⁶⁶ , Asp ¹⁸⁷	Arg ¹⁸⁸	Gly ¹⁴³ / * His ⁴¹
6	6-(ethylamino)-pyridine-3-carbonitrile	-3.57	Arg ¹⁸⁸	-	Met ⁴⁹ , Cys ¹⁴⁵ , Met ¹⁶⁵ , Leu ¹⁶⁷ , Pro ¹⁶⁸	His ⁴¹ , His ¹⁶⁴ , Gln ¹⁸⁹ , Thr ¹⁹⁰ , Gln ¹⁹²	Glu ¹⁶⁶ , Asp ¹⁸⁷	Arg ¹⁸⁸	Gly ¹⁴³

In molecular docked complexes, non-covalent interaction, such as electrostatic interactions, van der Waals interactions, salt bridges, hydrogen bonding, and metal interactions, are known to play a key role in the formation and stability of the receptor-ligand complex [58,59]. Remarkably, hydrogen bonding was reported to mediate the ligand binding with the receptor and fundamentally contribute to the physiochemical properties of the molecules, which are essentially required for the drug development of lead compounds [60,61]. Thus, each docked complex of natural products with SARS-CoV-2 M^{PRO} was studied for intermolecular interactions at 4 Å distance around the ligand with default parameters using the 2D interaction tool in Maestro-Schrödinger suite (Figure 4).

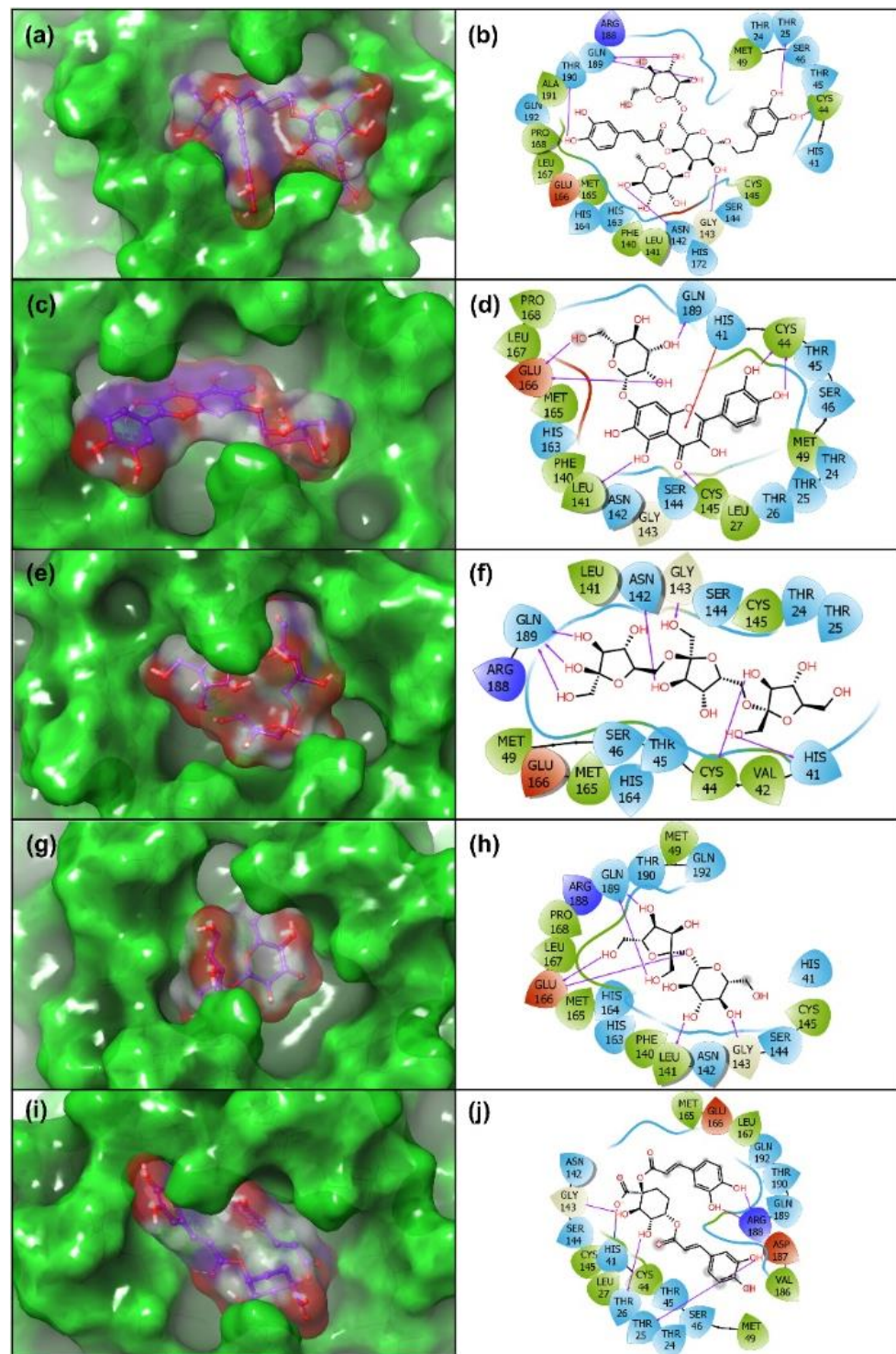


Figure 4. 3D and 2D interaction maps for the docked poses of SARS-CoV-2 M^{Pro} with potent natural products, i.e., (a,b) Echinacoside, (c,d) Quercetagenin 7-glucoside, (e,f) Levan N, (g,h) Inulin from chicory, and (i,j) 1,3-Dicaffeoylquinic acid. In 3D interaction poses, the docked ligand surface was generated based on partial charge while protein surface was rendered based on secondary structure. In 2D maps, hydrogen bond formation (pink arrows), hydrophobic (green), polar (blue), red (negative), violet (positive), glycine (grey), π - π stacking (green line), π -cation stacking (red line), and salt bridge (red-blue line), interactions are logged for docked complexes of SARS-CoV-2 M^{Pro} with selected natural products.

Molecular docked complexes of all the natural products, i.e., Echinacoside, Quercetagenin 7-glucoside, Levan N, Inulin from chicory, and 1,3-Dicaffeoylquinic acid, with SARS-CoV-2 M^{PRO} exhibited substantial binding affinity >10 kcal/mol against <4 kcal/mol binding energy for the reference compound, viz. 6-(ethylamino)pyridine-3-carbonitrile (Table 1). Additionally, a minimum of six hydrogen bond formation were observed for the selected natural products with active residues in the catalytic pocket of SARS-CoV-2 M^{PRO} by comparison to the reference compound (only one hydrogen bond formation with residue Arg¹⁸⁸). Of note, only SARS-CoV-2 M^{PRO}-Quercetagenin 7-glucoside and SARS-CoV-2 M^{PRO}-1,3-Dicaffeoylquinic acid docked complexes exhibited π -cation stacking (His⁴¹ residue) and salt bridge (His⁴¹ residue) formation (Figure 4). Additionally, substantial intermolecular interactions, such as hydrophobic, polar, negative, positive, π - π stacking, π -cation stacking, salt bridge, and glycine interactions, were noted in SARS-CoV-2 M^{PRO}-natural compounds against reference compound (Table 1, Figure 4, Figure S2). Interestingly, the interacting atoms of the respective ligands were predicted for molecular contacts with the active residues of the viral protease via electron donor and acceptor molecular contacts supporting the predicted sites on the respective optimized ligand geometries by DFT calculations for intermolecular interactions (Figure 3). Together, all the selected natural compounds were concluded as potent antagonists of SARS-CoV-2 M^{PRO} against reference compound 6-(ethylamino) pyridine-3-carbonitrile; this observation was also supported by significant intermolecular interaction profiles for the respective docked complexes.

3.4. Explicit Solvent Molecular Dynamics Simulation Analysis

Molecular dynamics simulation used in the drug discovery pipeline to establish the stability of small molecules docked with receptors computed from molecular docking simulations. The screened natural products docked with SARS-CoV-2 M^{PRO} were also evaluated for the complex stability and formation of intermolecular interactions against reference ligand with respect to 100 ns simulation interval. Initially, the ligands were observed for the steadiness in the binding pocket of the viral protease at the end of 100 ns MD simulation by comparison to the initial frame revealed considerable stability for all the natural products, except for SARS-CoV-2 M^{PRO}-1,3-Dicaffeoylquinic acid docked complex which showed displacement of ligand from the catalytic pocket (Figure 5). Moreover, in reference docked complex, i.e., SARS-CoV-2 M^{PRO}-6-(ethylamino) pyridine-3-carbonitrile, exhibited diffusion of ligand from the catalytic pocket into unknown cavity of the viral protease during 100 ns MD simulation against initial protein-receptor pose (Figure 5). Furthermore, each last pose extracted from respective 100 ns MD trajectory were analyzed for the intermolecular contacts formation between the ligand and essential residues in the catalytic pocket of SARS-CoV-2 M^{PRO} (Figures S3 and S4). Remarkably, all the natural products docked with viral protease were noted for the formation of substantial molecular contacts with the active residues in the catalytic pocket of viral protease, except for the reference ligand (Table S8). Of note, at least two hydrogen bonds and other intermolecular interactions between the active residues of viral protease and the selected natural products were observed, suggesting the inhibitory potential of selected natural compounds against catalytic activity of SARS-CoV-2 M^{PRO} (Table S8, Figure S3 and S4). To take further account on the respective docked complexes stability, root mean square deviation (RMSD), root mean square fluctuation (RMSF), and protein-ligand contacts maps were extracted from the respective 100 ns MD simulation trajectories.

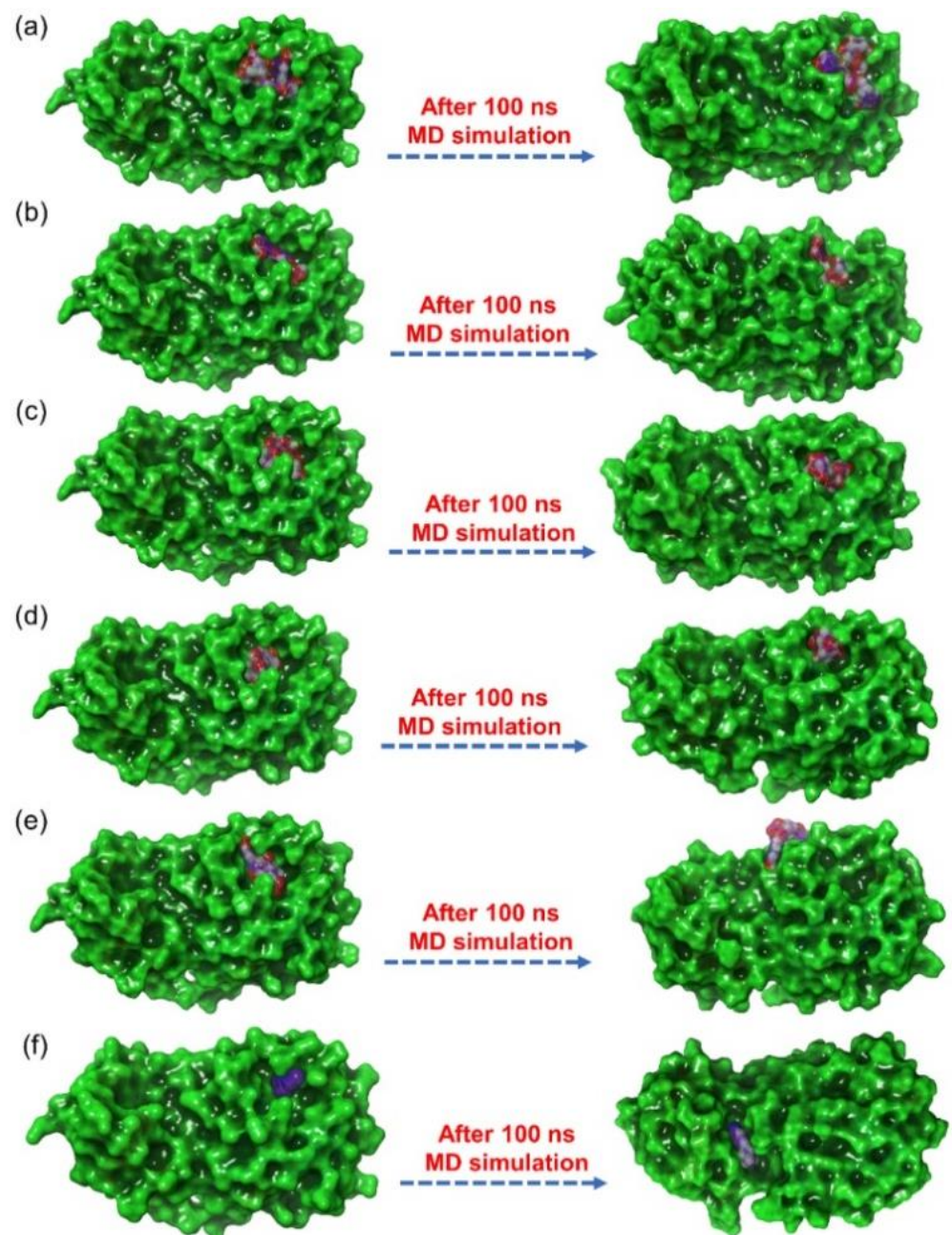


Figure 5. 3D docked poses of SARS-CoV-2 M^{Pro}-natural products, i.e., (a) Echinacoside, (b) Quercetagenin 7-glucoside, (c) Levan N, (d) Inulin from chicory, and (e) 1,3-Dicaffeoylquinic acid, and (f) 6-(ethylamino) pyridine-3-carbonitrile, exhibiting transition of docked poses through 100 ns MD simulation.

3.4.1. RMSD and RMSF Analysis

To calculate the average displacement in the protein and docked ligands in the respective complex during simulation interval, RMSD value for protein structure (C α , backbone, sidechain, and heavy) and protein fit ligand were computed in reference to initial frame of the MD simulation trajectory (Figure 6, Figures S5 and S6). Interestingly, all the protein structures in the docked complexes with selected natural products exhibited acceptable RMSD values (<2 Å) against reference ligand docked complex (<3 Å) till the end of 100 ns MD simulation (Figure 6, Figure S5). These observations suggested the stability of the viral protease in the docked state with selected natural products, supported by considerable RMSD values (<3 Å) of the backbone, sidechain, and heavy atoms in the SARS-CoV-2

M^{Pro} structure docked with respective natural products (Figure S6). Likewise, the protein fit ligand also showed deviations in the initial 10–50 ns interval and then followed by considerable variations and equilibrium state, except higher deviations were noticed for 1,3-Dicaffeoylquinic acid (<18.5 Å) till at the end of 100 ns simulation (Figure 6). Remarkably, only Quercetagenin 7-glucoside was observed with considerable deviations and acceptable RMSD (<3.5 Å) during 100 ns MD simulation interval (Figure 6, Figure S5). However, the reference ligand, i.e., 6-(ethylamino)pyridine-3-carbonitrile, docked with SARS-CoV-2 M^{Pro} exhibited higher RMSD (>50 Å) within 10 ns followed by deviations between 10–60 ns and a state of equilibrium (<30 Å) from 60 ns till end of the 100 ns simulation interval (Figure S5). The initial high deviation value indicated the diffusion of ligand from the receptor within time frame of 10 ns and later equilibrium state indicates the placement of ligand in the unknown cavity of the receptor as predicted in the last snapshot of respective 100 ns MD trajectory (Figure 5, Table S8). Hence, no further analysis was considered for the reference docked complex, i.e., SARS-CoV-2 M^{Pro}-6-(ethylamino)pyridine-3-carbonitrile. Moreover, RMSD values calculated for docked protein with natural products were further favored by acceptable RMSF values (<2 Å), except in the N- and C-terminal of the protein structure (<3.5 Å) (Figure S7). These end terminal fluctuations in the protein structure during the simulation can be ignored, which are far away from the catalytic pocket of the viral protease. Besides, natural products as fit ligand on protein also exhibited considerable RMSF values for the selected natural products, except in the atoms contributing molecular contacts with the active residues in the catalytic pocket of viral protease during the MD simulation interval (Figure S8). Collectively, although all the natural products were observed for stable complex formation with SARS-CoV-2 M^{Pro} but docked complex of SARS-CoV-2 M^{Pro}-Quercetagenin 7-glucoside demonstrated substantial stability against the other selected natural products and reference ligand.

3.4.2. Protein-Ligand Contact Mapping

In drug design, hydrogen bonding (backbone acceptor; backbone donor; side-chain acceptor; side-chain donor) plays a key function in the drug metabolism, adsorption, and drug specificity. Moreover, hydrophobic interactions (π -cation; π - π ; and other, and non-specific interactions), ionic interactions or polar interactions, and water bridge-hydrogen-bonded protein-ligand interactions mediated by a water molecule, also contributes to the stability of the docked complex during the simulation. Hence, intermolecular contact formed between SARS-CoV-2 M^{Pro} and docked natural products, i.e., were extracted from the respective MD trajectories using default parameters of the Desmond module (Figure 7).

Remarkably, all the docked natural products in the active pocket of SARS-CoV-2 M^{Pro} were observed substantial intermolecular contact formation with catalytic residues, i.e., His⁴¹ and Cys¹⁴⁵, and other substrate binding residues (Figure 7). Interestingly, these molecular contacts were also recorded in the respective docked complexes (Table 1, Figure 4), suggested the stability of docked complexes during simulation interval. Furthermore, all the natural products exhibited considerable number of intermolecular contacts, including hydrogen bonding, water bridging, hydrophobic, polar, negative, and positive interactions, with the active residues in the catalytic pocket of SARS-CoV-2 M^{Pro} during 30% of the total MD simulation interval, except for SARS-CoV-2 M^{Pro}-Echinacoside docked complex (Figure 8). However, no considerable interactions were noted for the reference complex as ligand moved out of the catalytic pocket during the initial phase of 100 ns MD simulation (Figure 5). Conclusively, analysis of the protein-ligand contact mapping suggested the considerable occupancy of selected natural products in the catalytic pocket of SARS-CoV-2 M^{Pro}. Hence, the natural products from *E. angustifolia* can be marked in the order, i.e., Quercetagenin 7-glucoside, Inulin from chicory, Levan N, 1,3-Dicaffeoylquinic acid, and Echinacoside, as potent inhibitor of SARS-CoV-2 M^{Pro} based on the number of intermolecular contacts formation during 30 % of the total 100 ns MD simulation interval.

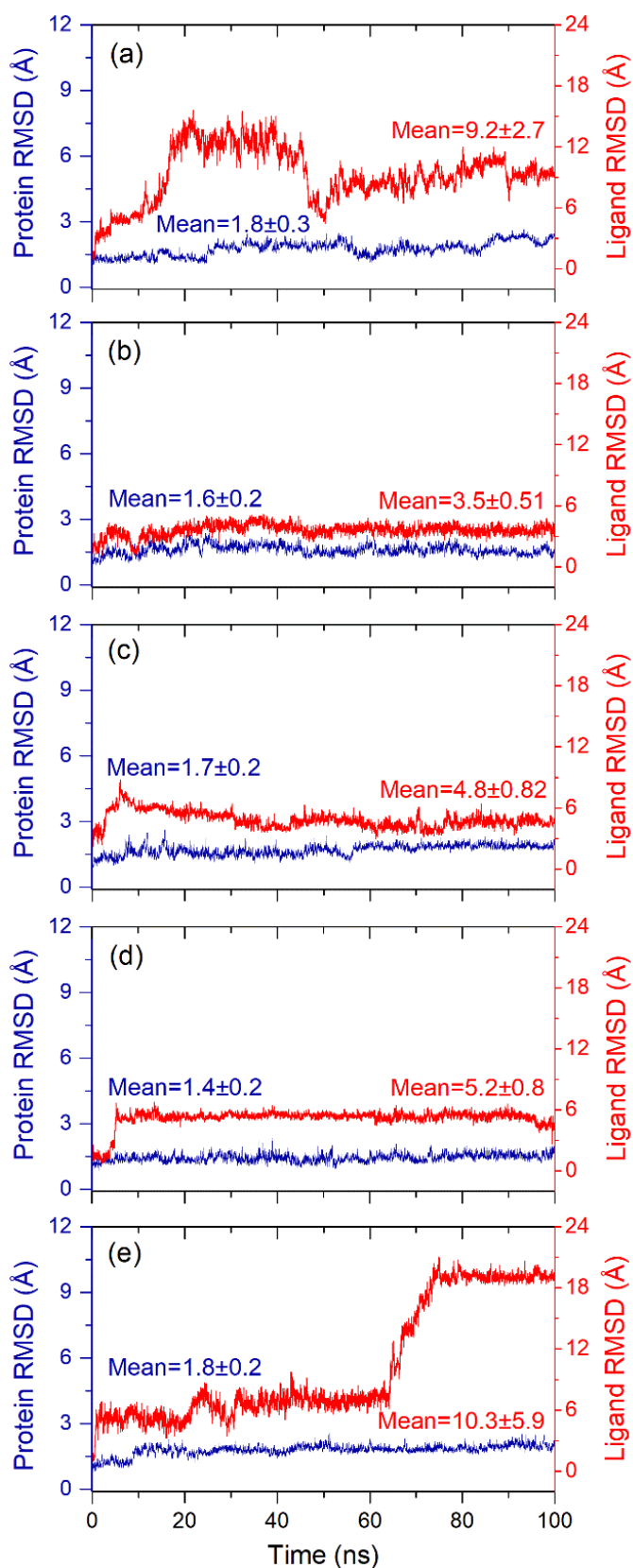


Figure 6. Root mean square deviation (RMSD) values plotted for alpha carbon atoms (blue curves) of SARS-CoV-2 M^{Pro} and natural products (red curves), i.e., (a) Echinacoside, (b) Quercetagenin 7-glucoside, (c) Levan N, (d) Inulin from chicory, and (e) 1,3-Dicaffeoylquinic acid, were extracted from 100 ns MD simulation interval of respective docked complexes.

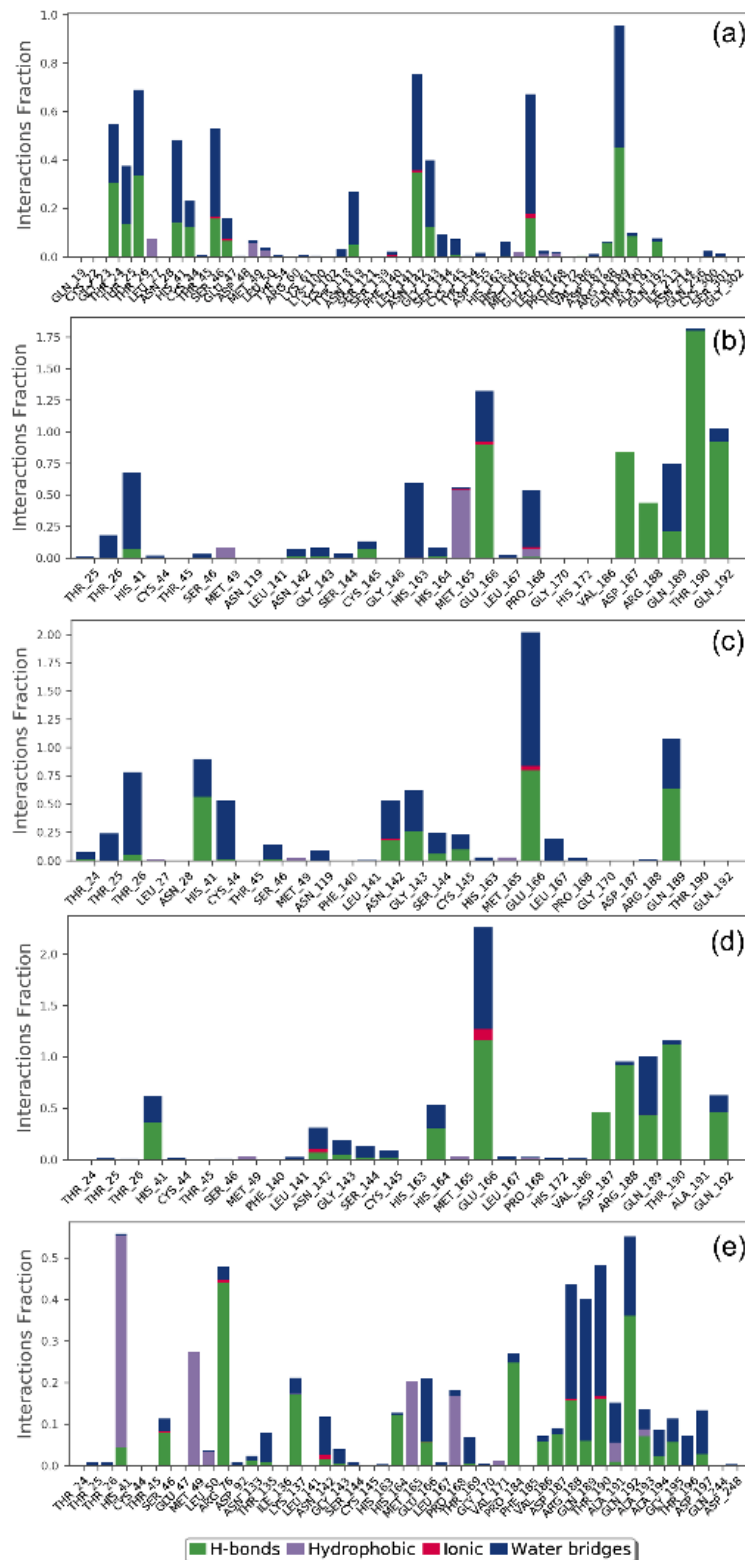


Figure 7. Protein-ligand interactions contact profiling for SARS-CoV-2 M^{Pro} docked with potential natural products, viz. (a) Echinacoside, (b) Quercetagenin 7-glucoside, (c) Levan N, (d) Inulin from chicory, and (e) 1,3-Dicaffeoylquinica acid, computed from 100 ns MD simulation trajectories.

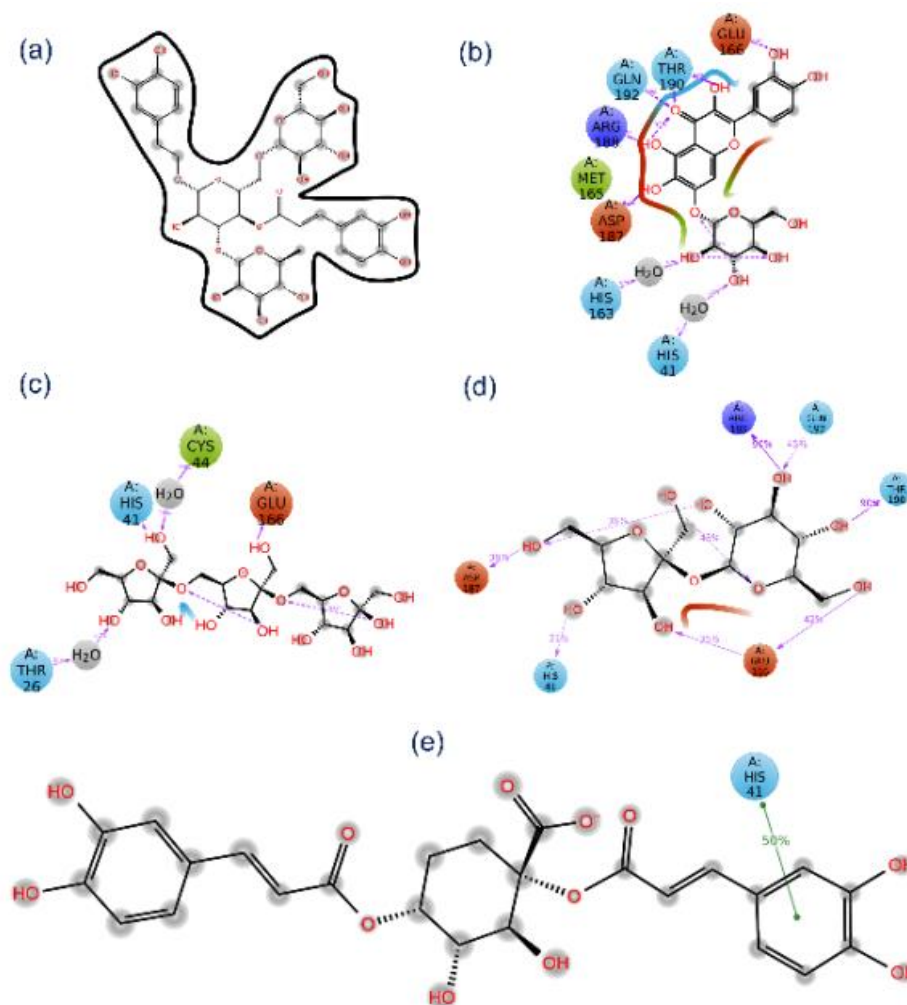


Figure 8. 2D interaction diagrams for docked SARS-CoV-2 M^{Pro}-potential natural products, i.e., (a) Echinacoside, (b) Quercetageitin 7-glucoside, (c) Levan N, (d) Inulin from chicory, and (e) 1,3-Dicaffeoylquinic acid, are generated at 30% of the total 100 ns MD simulation interaction interval.

3.5. Essential Dynamics Analysis

Essential dynamics is a statistical approach that assist in the extraction of the correlated motions in the protein structure in a trajectory produced by an MD simulation [28,62]. Thus, each simulation trajectory of docked SARS-CoV-2 M^{Pro} with potential natural products: (a) Echinacoside, (b) Quercetageitin 7-glucoside, (c) Levan N, (d) Inulin from chicory, and (e) 1,3-Dicaffeoylquinic acid, was used in the construction of covariance matrix after removal of the rotational motions. Following, the diagonalization of the matrix was generated using the Bio3D package which results in the production of a set of eigenvectors/eigenvalues (Figure 9). Herein, each eigenvector exhibits one single direction in a multidimensional space while the eigenvalue represents the amplitude of the motion along the eigenvector. Figure 9 shows all the complexes with a steep drop in eigen fraction corresponds to the early five eigen modes and represent ~60% displacement in the residual motion of protein; these results represent the considerable induced conformation fluctuations the protein structure because of docked natural products as ligand in the catalytic pocket of SARS-CoV-2 M^{Pro}. Interestingly, a successive elbow point at the 5th eigen value followed by no momentous variations in the eigen fraction demonstrated a state of convergence in the respective complexes (Figure 9). These observations suggested that a significant flexibility was produced in SARS-CoV-2 M^{Pro} during the initial phase of 100 ns MD simulation

which eventually diminished to attain a stable complex formation with the docked ligands. Moreover, a steady decrement in the amplitude of an eigen fraction further demonstrates an additional localized fluctuation in the protein structure to achieve a favorable conformation. Thus, these fluctuations recorded in each complex may be considered as a requirement for the stability of the respective docked complexes during MD simulation as function of time.

Moreover, the first three eigen vectors extracted from MD simulation trajectory of each selected complex were plotted to monitor the residual displacement in each protein structure where a color gradient change from blue to red stands through white color represents the periodic jumps among the extracted conformational poses of the docked protein structure (Figure 9). Of note, a considerable compact and variation in cluster distribution was observed for the residues of SARS-CoV-2 M^{Pro} during 100 ns simulation, except in SARS-CoV-2 M^{Pro}-1,3-Dicaffeoylquinic acid complex (Figure 9). Besides, SARS-CoV-2 M^{Pro}-Quercetagetin 7-glucoside and SARS-CoV-2 M^{Pro}-Inulin from chicory complexes exhibited most favorable converged conformations and limited variation against other docked complexes during MD simulation; suggesting the considerable complex stability as noted from the respective RMSD and RMSF values (Figure 6, Figures S7 and S8). Conclusively, the eventual decrease in correlated and compact motions in SARS-CoV-2 M^{Pro} structure in the respective docked complex demonstrates the induction of rigidity and complex stability of the respective complexes, except in residual motion induced by the docked ligand. In conclusion, a correlated fluctuations motion of the viral protease in all the studied systems represents the rigidity and the stability of the respective docked complexes, except in the SARS-CoV-2 M^{Pro}-1,3-Dicaffeoylquinic acid complex, during 100 ns MD simulation.

3.6. Binding Free Energy

Computational calculations for computing binding affinities have been suggested as rapid and the most cost-effective methods to predict the binding affinities by considering the dynamics nature of the protein-ligand interaction in end-point free binding energy calculations such as MD-based MMGBSA methods. Thus, free energy for the binding of selected ligands in the active pocket of SARS-CoV-2 M^{Pro} (ΔG_{Bind}) were calculated using the MMGBSA method [63], implemented in the Prime MM/GBSA module of Schrödinger Suite. Herein, average binding free energy for the extracted poses from the last 10 ns simulation interval of each 100 ns simulation trajectory (Figure 10), except for the reference compound which diffused from the binding pocket. Of note, all the selected docked complexes exhibited binding free energy >30 kcal/mol, maximum and minimum of binding free energy values were substantially noted for Quercetagetin 7-glucoside (-65.82 ± 2.74 kcal/mol) and 1,3-Dicaffeoylquinic acid (-42.57 ± 8.99 kcal/mol), respectively. Moreover, individual energy components contributing to net binding free energy, i.e., $\Delta G_{\text{Bind Coulomb}}$, $\Delta G_{\text{Bind Covalent}}$, $\Delta G_{\text{Bind Hbond}}$, $\Delta G_{\text{Bind Lipo}}$, $\Delta G_{\text{Bind Packing}}$, $\Delta G_{\text{Bind Solv GB}}$ and $\Delta G_{\text{Bind vdW}}$ were also computed in the MM/GBSA method (Figure 10, Table S9). Remarkably, $\Delta G_{\text{Bind Coulomb}}$ and $\Delta G_{\text{Bind vdW}}$ were logged as the main contributors to the binding free energy for each ligand binding with the viral protease while $\Delta G_{\text{Bind Covalent}}$ and $\Delta G_{\text{Bind Solv GB}}$ were noted for contribution in unfavorable energy, therefore, reducing the net binding free energy values for each docked complex. These results agreed with a recent MMGBSA results for SARS-CoV-2 M^{Pro} with Food and Drug Administration (FDA) approved drugs, in which $\Delta G_{\text{Bind Coulomb}}$ and $\Delta G_{\text{Bind vdW}}$ showed maximum contribution in the stabilization of the docked complexes [64]. Collectively, the selected natural products were deduced with substantial stability in the active pocket of viral protease as predicted from molecular docking and MD simulation analysis.

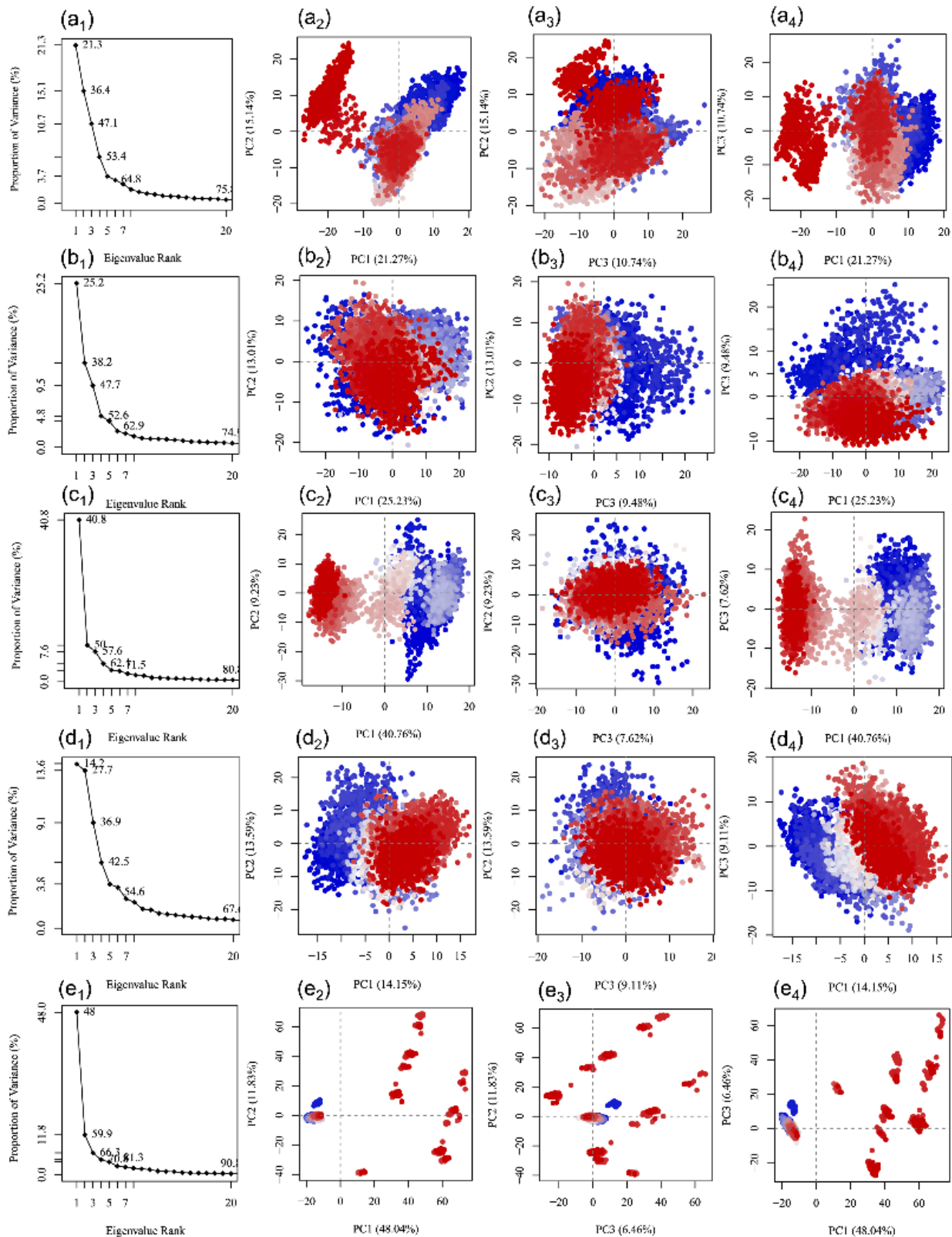


Figure 9. Principal component analysis for SARS-CoV-2 docked complexes with natural products, i.e., (a) Echinacoside, (b) Quercetagenin 7-glucoside, (c) Levan N, (d) Inulin from chicory, and (e) 1,3-Dicaffeoylquinic acid. The change from blue to red through white color in respective scatter plots shows the periodic jumps in the different conformations of the viral protease during 100 ns MD simulation intervals.

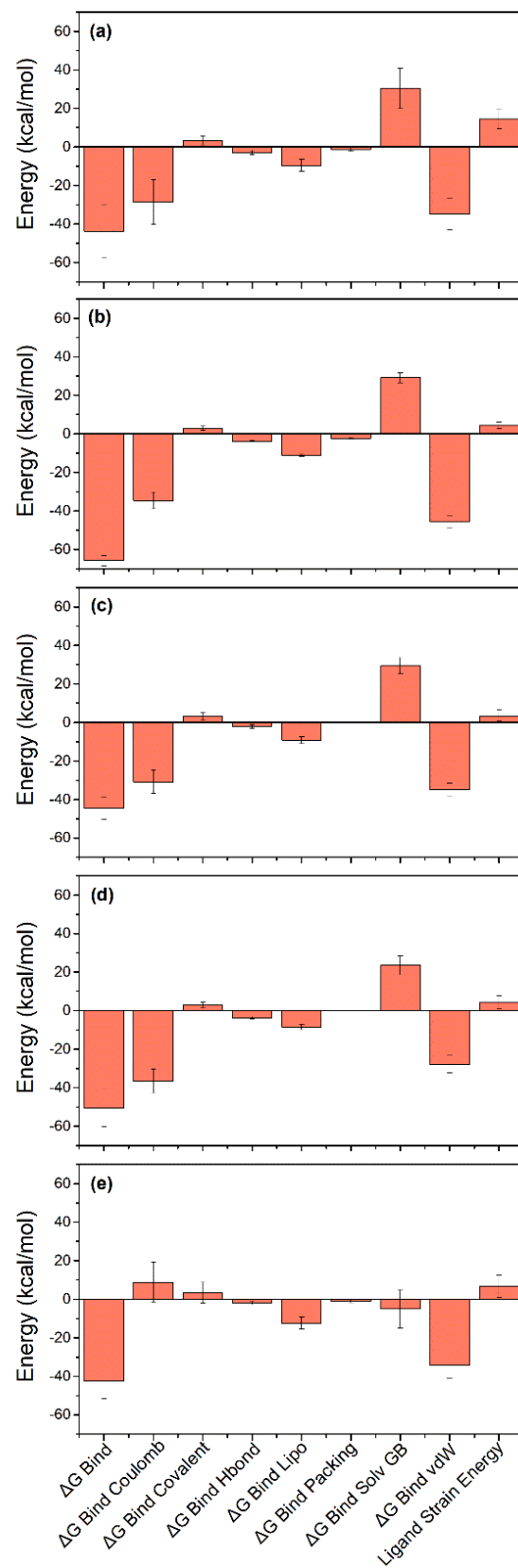


Figure 10. Average binding free energy and their dissociation energy components calculated for the extracted poses of SARS-CoV-2 M^{pro} with potent natural products, i.e., (a) Echinacoside, (b) Quercetagenin 7-glucoside, (c) Levan N, (d) Inulin from chicory, and (e) 1,3-Dicaffeoylquinic acid, from respective 100 ns MD trajectories.

4. Conclusions

This study aimed to identify the potent anti-SARS-CoV-2 compounds from *E. angustifolia* via SARS-CoV-2 M^{Pro} inhibition through computational approaches. A total of five natural products were selected, i.e., Echinacoside, Quercetagenin 7-glucoside, Levan N, Inulin from chicory, and 1,3-Dicaffeoylquinic acid, based on substantial binding energy with catalytic pocket of SARS-CoV-2 M^{Pro}. Eventually, the selected natural products were noted with considerable bioactivity and formation of strong molecular contacts with the conserved residues in the catalytic pocket of the SARS-CoV-2 M^{Pro}, supported by molecular dynamics simulation and post simulation analysis. Based on the computed binding affinities, the selected compounds exhibited a potential inhibitory activity against the SARS-CoV-2 M^{Pro} and can be used as potent antivirals against SARS-CoV-2 infection. This study provided an important step in the exploration of natural products from medical herbs for structure-based design of anti-SARS-CoV-2 drugs.

Supplementary Materials: The following are available online at <https://www.mdpi.com/1999-4915/13/2/305/s1>, Figure S1. Molecular orbitals LUMO and HOMO of the optimized reference compound 6-(ethylamino)pyridine-3-carbonitrile calculated using theoretical model B3LYP/6-31G, Figure S2. 2D interaction maps for the docked poses of SARS-CoV-2 M^{Pro} with reference compound 6-(ethylamino)pyridine-3-carbonitrile, Figure S3. 2D interaction maps for the docked poses of SARS-CoV-2 M^{Pro} with potent compounds, Figure S4. 2D interaction maps for the docked poses of SARS-CoV-2 M^{Pro} with reference compound 6-(ethylamino)pyridine-3-carbonitrile after MD simulation, Figure S5. RMSD values plotted for alpha carbon atoms (blue curves) of SARS-CoV-2 M^{Pro} and reference ligand 6-(ethylamino)pyridine-3-carbonitrile (red curves) for the respective docked complexes extracted from 100 ns MD simulation interval, Figure S6. RMSD values plotted for Protein Backbone, Sidechains, and heavy Atoms in docked state, Figure S7. RMSF values plotted for alpha carbon atoms of SARS-CoV-2 M^{Pro} docked with natural products, Figure S8. RMSF values plotted for the natural products, Table S1. List of natural products from *Echinacea angustifolia* docked by extra precision method at the active pocket of SARS-CoV-2 M^{Pro}, Table S2. Optimized geometry parameters for the natural product Echinacoside, Table S3. Optimized geometry parameters for the natural product Quercetagenin 7-Glucoside, Table S4. Optimized geometry parameters for the natural product Levan N, Table S5: Optimized geometry parameters for the natural product Inulin from chicory, Table S5. Optimized geometry parameters for the natural product Inulin from chicory, Table S6. Optimized geometry parameters for the natural product 1,3-Dicaffeoylquinic Acid, Table S7. Optimized geometry parameters for the reference compound 6-(ethylamino)pyridine-3-carbonitrile, Table S8. List of interactions and residues at the active pocket of viral protease interacting with the potential natural compounds logged from respective docked complexes after 100 ns simulation, Table S9 Averaged binding free energies (kcal/mol) and their components calculated using MM/GBSA method for all the selected natural products docked with SARS-CoV-2 M^{Pro}.

Author Contributions: Conceptualization, S.B., E.I.A., V.D.D. and S.G.K.; methodology, S.B., S.A.E.-K., and T.A.A.; software, A.K.S., and U.Y.; validation, S.B., M.A.K., E.I.A., S.G.K. and V.D.D.; formal analysis, S.B., L.H.B., A.D.; investigation, S.B., A.D. and V.D.D.; resources, S.B., and A.A.S.; data curation, S.B.; writing—original draft preparation, S.B., S.A.E.-K. and T.A.A.; writing—review and editing, S.B.; visualization, S.B.; supervision, E.I.A., S.G.K., and V.D.D.; project administration, E.I.A., S.G.K., and V.D.D.; funding acquisition, E.I.A. All authors have read and agreed to the published version of the manuscript.

Funding: This project was funded by the Deanship of Scientific Research (DSR) at King Abdulaziz University, Jeddah under Grant Number GCV19-47-1441. The authors therefore acknowledge with thanks DSR for financial and technical support. The funders had no role in the design of the study; in the collection, analyses, or interpretation of data; in the writing of the manuscript, or in the decision to publish the results.

Institutional Review Board Statement: Not applicable.

Informed Consent Statement: Not applicable.

Data Availability Statement: Data are available in the article and in the Supplementary Materials.

Conflicts of Interest: The authors declare no conflict of interest.

References

1. Kirtipal, N.; Bharadwaj, S.; Kang, S.G. From SARS to SARS-CoV-2, insights on structure, pathogenicity and immunity aspects of pandemic human coronaviruses. *Infect. Genet. Evol.* **2020**, *85*, 104502. [[CrossRef](#)]
2. Coronavirus, N. *Novel Coronavirus (2019-nCoV) Situation Reports—World Health Organization*; WHO: Geneva, Switzerland, 2020.
3. Zhang, L.; Lin, D.; Sun, X.; Curth, U.; Drosten, C.; Sauerhering, L.; Becker, S.; Rox, K.; Hilgenfeld, R. Crystal structure of SARS-CoV-2 main protease provides a basis for design of improved alpha-ketoamide inhibitors. *Science* **2020**, *368*, 409–412. [[CrossRef](#)] [[PubMed](#)]
4. Zhang, L.; Lin, D.; Kusov, Y.; Nian, Y.; Ma, Q.; Wang, J.; von Brunn, A.; Leyssen, P.; Lanko, K.; Neyts, J.; et al. α -Ketoamides as broad-spectrum inhibitors of coronavirus and enterovirus replication: Structure-based design, synthesis, and activity assessment. *J. Med. Chem.* **2020**, *63*, 4562–4578. [[CrossRef](#)]
5. Ma, Y.; Zhao, Y.; Liu, J.; He, X.; Wang, B.; Fu, S.; Yan, J.; Niu, J.; Zhou, J.; Luo, B. Effects of temperature variation and humidity on the death of COVID-19 in Wuhan, China. *Sci. Total. Environ.* **2020**, *724*, 138226. [[CrossRef](#)] [[PubMed](#)]
6. Arya, A.; Dwivedi, V.D. Synergistic effect of vitamin D and Remdesivir can fight COVID-19. *J. Biomol. Struct. Dyn.* **2020**, 1–2. [[CrossRef](#)] [[PubMed](#)]
7. Dwivedi, V.D.; Tripathi, I.P.; Mishra, S.K. In silico evaluation of inhibitory potential of triterpenoids from *Azadirachta indica* against therapeutic target of dengue virus, NS2B-NS3 protease. *J. Vector Borne Dis.* **2016**, *53*, 156–161.
8. Benarba, B.; Pandiella, A. Medicinal plants as sources of active molecules against COVID-19. *Front. Pharmacol.* **2020**, *11*, 1189. [[CrossRef](#)]
9. Joseph, J.; Thankamani, K.; Ajay, A.; Das, V.R.A.; Raj, V.S. Green tea and *Spirulina* extracts inhibit SARS, MERS, and SARS-2 spike pseudotyped virus entry in vitro. *BioRxiv* **2020**. [[CrossRef](#)]
10. Signer, J.; Jonsdottir, H.R.; Albrich, W.C.; Strasser, M.; Züst, R.; Ryter, S.; Ackermann-Gaumann, R.; Lenz, N.; Siegrist, D.; Suter, A.; et al. In Vitro virucidal activity of Echinaforce[®], an *Echinacea purpurea* preparation, against coronaviruses, including common cold coronavirus 229E and SARS-CoV-2. *Virology* **2020**, *17*, 136. [[CrossRef](#)]
11. Aucoin, M.; Cooley, K.; Saunders, P.R.; Carè, J.; Anheyser, D.; Medina, D.N.; Cardozo, V.; Remy, D.; Hannan, N.; Garber, A. The effect of *Echinacea* spp. on the prevention or treatment of COVID-19 and other respiratory tract infections in humans: A rapid review. *Adv. Integr. Med.* **2020**, *7*, 203–217. [[CrossRef](#)]
12. Kembuan, G.; Lie, W.; Tumimomor, A. Potential usage of immune modulating supplements of the *Echinacea* genus for COVID-19 infection. *Int. J. Med. Rev. Case Rep.* **2020**, *4*. [[CrossRef](#)]
13. Hudson, J.; Vimalanathan, S. *Echinacea*—A source of potent antivirals for respiratory virus infections. *Pharmaceuticals* **2011**, *4*, 1019–1031. [[CrossRef](#)]
14. Barnes, J.; Anderson, L.A.; Gibbons, S.; Phillipson, J.D. *Echinacea* species (*Echinacea angustifolia* (DC.) Hell., *Echinacea pallida* (Nutt.) Nutt., *Echinacea purpurea* (L.) Moench): A review of their chemistry, pharmacology and clinical properties. *J. Pharm. Pharmacol.* **2005**, *57*, 929–954. [[CrossRef](#)]
15. Barrett, B. Medicinal properties of *Echinacea*: A critical review. *Phytomedicine* **2003**, *10*, 66–86. [[CrossRef](#)]
16. Rehman, F.; Sudhaker, M.; Roshan, S.; Khan, A. Antibacterial activity of *Echinacea angustifolia*. *Pharmacogn. J.* **2012**, *4*, 67–70. [[CrossRef](#)]
17. Hudson, J.; Vimalanathan, S.; Kang, L.; Amiguet, V.T.; Livesey, J.; Arnason, J.T. Characterization of antiviral activities in *Echinacea*. Root preparations. *Pharm. Biol.* **2005**, *43*, 790–796. [[CrossRef](#)]
18. Fearon, D.; Powell, A.J.; Douangamath, A.; Owen, C.D.; Wild, C.; Krojer, T.; Lukacik, P.; Strain-Damerell, C.M.; Walsh, M.A.; von Delft, F. PanDDA analysis of COVID-19 main protease against the DSI-poised Fragment Library. Unpublished work. 2020.
19. Erbel, P.; Schiering, N.; D’Arcy, A.; Renatus, M.; Kroemer, M.; Lim, S.P.; Yin, Z.; Keller, T.H.; Vasudevan, S.G.; Hommel, U. Structural basis for the activation of flaviviral NS3 proteases from dengue and West Nile virus. *Nat. Struct. Mol. Biol.* **2006**, *13*, 372–373. [[CrossRef](#)] [[PubMed](#)]
20. Kim, S.; Thiessen, P.A.; Bolton, E.E.; Chen, J.; Fu, G.; Gindulyte, A.; Han, L.; He, J.; He, S.; Shoemaker, B.A. PubChem substance and compound databases. *Nucleic Acids Res.* **2015**, *44*, D1202–D1213. [[CrossRef](#)]
21. Friesner, R.A.; Murphy, R.B.; Repasky, M.P.; Frye, L.L.; Greenwood, J.R.; Halgren, T.A.; Sanschagrin, P.C.; Mainz, D.T. Extra precision glide: Docking and scoring incorporating a model of hydrophobic enclosure for protein–ligand complexes. *J. Med. Chem.* **2006**, *49*, 6177–6196. [[CrossRef](#)] [[PubMed](#)]
22. Fukuda, R.; Hasegawa, J.; Ishida, M.; Nakajima, T.; Honda, Y.; Kitao, O.; Nakai, H.; Klene, M.; Li, X.; Knox, J.E. *Gaussian 03, Revision, B. 04*; Gaussian, Inc.: Wallingford, CT, USA, 2003.
23. Kohn, W.; Sham, L.J. Self-consistent equations including exchange and correlation effects. *Phys. Rev.* **1965**, *140*, A1133–A1138. [[CrossRef](#)]
24. Lee, C.; Yang, W.; Parr, R.G. Development of the Colle-Salvetti correlation-energy formula into a functional of the electron density. *Phys. Rev. B* **1988**, *37*, 785–789. [[CrossRef](#)] [[PubMed](#)]
25. Miehlich, B.; Savin, A.; Stoll, H.; Preuss, H. Results obtained with the correlation energy density functionals of becke and Lee, Yang and Parr. *Chem. Phys. Lett.* **1989**, *157*, 200–206. [[CrossRef](#)]

26. Bharadwaj, S.; Lee, K.E.; Dwivedi, V.D.; Yadava, U.; Nees, M.; Kang, S.G. Density functional theory and molecular dynamics simulation support Ganoderma lucidum triterpenoids as broad range antagonist of matrix metalloproteinases. *J. Mol. Liq.* **2020**, *311*, 113322. [[CrossRef](#)]
27. Bowers, K.J.; Chow, D.E.; Xu, H.; Dror, R.O.; Eastwood, M.P.; Gregersen, B.A.; Klepeis, J.L.; Kolossvary, I.; Moraes, M.A.; Sacerdoti, F.D.; et al. Scalable algorithms for molecular dynamics simulations on commodity clusters. In Proceedings of the ACM/IEEE SC 2006 Conference (SC'06), Tampa, FL, USA, 11–17 November 2006; IEEE: Piscataway, NJ, USA, 2006; p. 43. [[CrossRef](#)]
28. Amadei, A.; Linssen, A.B.M.; Berendsen, H.J.C. Essential dynamics of proteins. *Proteins Struct. Funct. Bioinform.* **1993**, *17*, 412–425. [[CrossRef](#)]
29. Daidone, I.; Amadei, A. Essential dynamics: Foundation and applications. *Wiley Interdiscip. Rev. Comput. Mol. Sci.* **2012**, *2*, 762–770. [[CrossRef](#)]
30. Grant, B.J.; Rodrigues, A.P.C.; ElSawy, K.M.; McCammon, J.A.; Caves, L.S.D. Bio3d: An R package for the comparative analysis of protein structures. *Bioinformatics* **2006**, *22*, 2695–2696. [[CrossRef](#)]
31. R Core Team. *R: A Language and Environment for Statistical Computing*; R Foundation for Statistical Computing: Vienna, Austria, 2013.
32. Wang, E.; Sun, H.; Wang, J.; Wang, Z.; Liu, H.; Zhang, J.Z.H.; Hou, T. End-point binding free energy calculation with MM/PBSA and MM/GBSA: Strategies and applications in drug design. *Chem. Rev.* **2019**, *119*, 9478–9508. [[CrossRef](#)]
33. Mena-Ulecia, K.; Tiznado, W.; Caballero, J. Study of the differential activity of thrombin inhibitors using docking, QSAR, molecular dynamics, and MM-GBSA. *PLoS ONE* **2015**, *10*, e0142774. [[CrossRef](#)]
34. Bharadwaj, S.; Rao, A.K.; Dwivedi, V.D.; Mishra, S.K.; Yadava, U. Structure-based screening and validation of bioactive compounds as Zika virus methyltransferase (MTase) inhibitors through first-principle density functional theory, classical molecular simulation and QM/MM affinity estimation. *J. Biomol. Struct. Dyn.* **2020**, 1–14. [[CrossRef](#)]
35. Genheden, S.; Kuhn, O.; Mikulskis, P.; Hoffmann, D.; Ryde, U. The normal-mode entropy in the MM/GBSA method: Effect of system truncation, buffer region, and dielectric constant. *J. Chem. Inf. Model.* **2012**, *52*, 2079–2088. [[CrossRef](#)]
36. Ben-Shalom, I.Y.; Pfeiffer-Marek, S.; Baringhaus, K.-H.; Gohlke, H. Efficient approximation of ligand rotational and translational entropy changes upon binding for use in MM-PBSA calculations. *J. Chem. Inf. Model.* **2017**, *57*, 170–189. [[CrossRef](#)]
37. Duan, L.; Liu, X.; Zhang, J.Z. Interaction entropy: A new paradigm for highly efficient and reliable computation of protein–ligand binding free energy. *J. Am. Chem. Soc.* **2016**, *138*, 5722–5728. [[CrossRef](#)]
38. Genheden, S.; Akke, M.; Ryde, U. Conformational entropies and order parameters: Convergence, reproducibility, and transferability. *J. Chem. Theory Comput.* **2014**, *10*, 432–438. [[CrossRef](#)]
39. Hikiri, S.; Yoshidome, T.; Ikeguchi, M. Computational methods for configurational entropy using internal and cartesian coordinates. *J. Chem. Theory Comput.* **2016**, *12*, 5990–6000. [[CrossRef](#)] [[PubMed](#)]
40. Sharp, K. Calculation of molecular entropies using temperature integration. *J. Chem. Theory Comput.* **2012**, *9*, 1164–1172. [[CrossRef](#)]
41. Choi, H.; Kang, H.; Park, H. Computational Prediction of molecular hydration entropy with hybrid scaled particle theory and free-energy perturbation method. *J. Chem. Theory Comput.* **2015**, *11*, 4933–4942. [[CrossRef](#)]
42. Gyimesi, G.; Závodszy, P.; Szilágyi, A. Calculation of Configurational entropy differences from conformational ensembles using gaussian mixtures. *J. Chem. Theory Comput.* **2016**, *13*, 29–41. [[CrossRef](#)] [[PubMed](#)]
43. Hou, T.; Wang, J.; Li, Y.; Wang, W. Assessing the performance of the MM/PBSA and MM/GBSA methods. II. The accuracy of binding free energy calculations based on molecular dynamics simulations. *J. Chem. Inf. Model.* **2010**, *51*, 69–82. [[CrossRef](#)]
44. Cheminat, A.; Zawatzky, R.; Becker, H.; Brouillard, R. Caffeoyl conjugates from *Echinacea* species: Structures and biological activity. *Phytochemistry* **1988**, *27*, 2787–2794. [[CrossRef](#)]
45. Vohra, S.; Adams, D.; Hudson, J.; Moore, J.; Vimalanathan, S.; Sharma, M.; Burt, A.; Lamont, E.; Lacaze, N.; Arnason, J.; et al. Selection of natural health products for clinical trials: A preclinical template. *Can. J. Physiol. Pharmacol.* **2009**, *87*, 371–378. [[CrossRef](#)] [[PubMed](#)]
46. Meyer, D. Chapter Two—Health benefits of prebiotic fibers. In *Advances in Food and Nutrition Research*; Henry, J., Ed.; Academic Press: Cambridge, MA, USA, 2015; Volume 74, pp. 47–91.
47. Srikanth, R.; Reddy, C.H.; Siddartha, G.; Ramaiah, M.J.; Uppuluri, K.B. Review on production, characterization and applications of microbial levan. *Carbohydr. Polym.* **2015**, *120*, 102–114. [[CrossRef](#)]
48. Esawy, M.A.; Ahmed, E.F.; Helmy, W.A.; Mansour, N.M.; El-Senousy, W.M.; El-Safty, M.M. Production of levansucrase from novel honey *Bacillus subtilis* isolates capable of producing antiviral levans. *Carbohydr. Polym.* **2011**, *86*, 823–830. [[CrossRef](#)]
49. Peiris, M. Pathogenesis of Avian flu H5N1 and SARS. *Novartis Found. Symp.* **2006**, *279*, 56–65.
50. Wan, X.; Guo, H.; Liang, Y.; Zhou, C.; Liu, Z.; Li, K.; Niu, F.; Zhai, X.; Wang, L. The physiological functions and pharmaceutical applications of inulin: A review. *Carbohydr. Polym.* **2020**, *246*, 116589. [[CrossRef](#)] [[PubMed](#)]
51. Lee, J.-B.; Miyake, S.; Umetsu, R.; Hayashi, K.; Chijimatsu, T.; Hayashi, T. Anti-influenza A virus effects of fructan from Welsh onion (*Allium fistulosum* L.). *Food Chem.* **2012**, *134*, 2164–2168. [[CrossRef](#)] [[PubMed](#)]
52. Danino, O.; Gottlieb, H.E.; Grossman, S.; Bergman, M. Antioxidant activity of 1,3-dicaffeoylquinic acid isolated from *Inula visosa*. *Food Res. Int.* **2009**, *42*, 1273–1280. [[CrossRef](#)]
53. Slanina, J.; Táborská, E.; Bochořáková, H.; Slaninová, I.; Humpa, O.; Robinson, W.; Schram, K.H. New and facile method of preparation of the anti-HIV-1 agent, 1,3-dicaffeoylquinic acid. *Tetrahedron Lett.* **2001**, *42*, 3383–3385. [[CrossRef](#)]

54. Li, L.; Chang, S.; Xiang, J.; Li, Q.; Liang, H.; Tang, Y.; Liu, Y. Screen anti-influenza lead compounds that target the PA C subunit of H5N1 viral RNA polymerase. *PLoS ONE* **2012**, *7*, e35234.
55. Fukui, K. The role of frontier orbitals in chemical reactions (Nobel Lecture). *Angew. Chem. Int. Ed.* **1982**, *21*, 801–809. [[CrossRef](#)]
56. Pearson, R.G. Electronic spectra and chemical reactivity. *J. Am. Chem. Soc.* **1988**, *110*, 2092–2097. [[CrossRef](#)]
57. Thanthiriwatte, K.S.; De Silva, K.N. Non-linear optical properties of novel fluorenyl derivatives—Ab initio quantum chemical calculations. *J. Mol. Struct. THEOCHEM* **2002**, *617*, 169–175. [[CrossRef](#)]
58. Gohlke, H.; Klebe, G. Approaches to the description and prediction of the binding affinity of small-molecule ligands to macromolecular receptors. *Angew. Chem. Int. Ed. Engl.* **2002**, *41*, 2644–2676. [[CrossRef](#)]
59. Thangavel, M.; Chandramohan, V.; Shankaraiah, L.H.; Jayaraj, R.L.; Poomani, K.; Magudeeswaran, S.; Govindasamy, H.; Vijayakumar, R.; Rangasamy, B.; Dharmar, M. Design and molecular dynamic Investigations of 7, 8-Dihydroxyflavone derivatives as potential neuroprotective agents against alpha-synuclein. *Sci. Rep.* **2020**, *10*, 1–10.
60. Connelly, P.R.; Snyder, P.W.; Zhang, Y.; McClain, B.; Quinn, B.P.; Johnston, S.; Medek, A.; Tanoury, J.; Griffith, J.; Walters, W.P.; et al. The potency–insolubility conundrum in pharmaceuticals: Mechanism and solution for hepatitis C protease inhibitors. *Biophys. Chem.* **2015**, *196*, 100–108. [[CrossRef](#)]
61. Sanphui, P.; Rajput, L.; Gopi, S.P.; Desiraju, G.R. New multi-component solid forms of anti-cancer drug Erlotinib: Role of auxiliary interactions in determining a preferred conformation. *Acta Crystallogr. Sect. B Struct. Sci. Cryst. Eng. Mater.* **2016**, *72*, 291–300. [[CrossRef](#)]
62. Brigo, A.; Lee, K.W.; Mustata, G.I.; Briggs, J.M. Comparison of multiple molecular dynamics trajectories calculated for the drug-resistant HIV-1 integrase T66I/M154I catalytic domain. *Biophys. J.* **2005**, *88*, 3072–3082. [[CrossRef](#)] [[PubMed](#)]
63. Tsui, V.; Case, D.A. Theory and applications of the generalized Born solvation model in macromolecular simulations. *Biopolymers* **2000**, *56*, 275–291. [[CrossRef](#)]
64. Bharadwaj, S.; Azhar, E.I.; Kamal, M.A.; Bajrai, L.H.; Dubey, A.; Jha, K.; Yadava, U.; Kang, S.G.; Dwivedi, V.D. SARS-CoV-2 M(pro) inhibitors: Identification of anti-SARS-CoV-2 M(pro) compounds from FDA approved drugs. *J. Biomol. Struct. Dyn.* **2020**, 1–16. [[CrossRef](#)]